Active elastic thin shell theory for cellular deformations

2014 New J. Phys. 16 065005

(http://iopscience.iop.org/1367-2630/16/6/065005)

New Journal of Physics
The open access journal at the forefront of physics
Deutsche Physikalische Gesellschaft DPG | IOP Institute of Physics

Active elastic thin shell theory for cellular deformations

Hélène Berthoumieux[1,2,3], Jean-Léon Maître[4,5], Carl-Philipp Heisenberg[4], Ewa K Paluch[6], Frank Jülicher[1] and Guillaume Salbreux[1]

[1] Max Planck Institute for the Physics of Complex Systems, Nöthnitzerstr. 38, 01187 Dresden, Germany
[2] Sorbonne Universités, UPMC Univ Paris 06, UMR 7600, LPTMC, F-75005, Paris, France
[3] CNRS, UMR 7600, LPTMC, F-75005, Paris, France
[4] Institute of Science and Technology Austria, Klosterneuburg, Austria
[5] EMBL, Meyerhofstrasse 1, 69117 Heidelberg, Germany
[6] MRC LMCB, University College London, Gower Street, WC1E 6BT, London, UK
E-mail: salbreux@pks.mpg.de

Received 24 October 2013, revised 18 February 2014
Accepted for publication 12 March 2014
Published 10 June 2014

New Journal of Physics **16** (2014) 065005

doi:10.1088/1367-2630/16/6/065005

Abstract

We derive the equations for a thin, axisymmetric elastic shell subjected to an internal active stress giving rise to active tension and moments within the shell. We discuss the stability of a cylindrical elastic shell and its response to a localized change in internal active stress. This description is relevant to describe the cellular actomyosin cortex, a thin shell at the cell surface behaving elastically at a short timescale and subjected to active internal forces arising from myosin molecular motor activity. We show that the recent observations of cell deformation following detachment of adherent cells (Maître J-L *et al* 2012 *Science* **338** 253–6) are well accounted for by this mechanical description. The actin cortex elastic and bending moduli can be obtained from a quantitative analysis of cell shapes observed in these experiments. Our approach thus provides a non-invasive, imaging-based method for the extraction of cellular physical parameters.

Keywords: active matter, elastic shell theory, cytoskeleton, cell adhesion

1. Introduction

Living systems have the ability to generate internal forces from the energy provided by adenosine triphosphate (ATP) consumption. Inside the cell, the main generator of forces are molecular motors binding to networks of filaments forming the cytoskeleton. The cellular actin cortex is one of the essential cytoskeletal structures: it is a thin shell of actin filaments and molecular motors connected to the cell membrane, playing an essential role in controlling cell shape [1].

Actin filamentous networks are generally viscoelastic, with elastic properties at short timescales and viscous properties at long timescales, as the network rearranges and dissipates stresses. We discuss here the properties of the actin cortex in the limit of short time scales, for which actin networks behave elastically. For the sake of simplicity, we assume that the network elastic material properties are isotropic. The actin cortex can then be represented by an active elastic material, whose constitutive equation for the stress can be written for small deformations [2]

$$\sigma_{\alpha\beta} = \frac{E}{1+\nu}\left(a_{\alpha\beta} + \frac{\nu}{1-2\nu}a_{\gamma\gamma}\delta_{\alpha\beta}\right) + \zeta_{\alpha\beta}, \tag{1}$$

such that the stress has two contributions: the first part is an elastic stress arising from the symmetric part of the deformation gradient $a_{\alpha\beta}$, and the second term $\zeta_{\alpha\beta}$ is an internal stress arising from active processes in the material. The elastic stress depends on the Young's modulus E and the Poisson ratio ν of the filamentous network. The Poisson ratio has to take values between -1 and $\frac{1}{2}$ for the undeformed material to be stable. The active stress $\zeta_{\alpha\beta}$ arises from out-of-equilibrium cellular processes consuming ATP. In cellular actin networks, myosin molecular motors, which hydrolyze ATP and use the released energy to slide actin filaments with respect to each other, are the key examples of processes that introduce active stresses. The active stress is introduced in addition to the passive elastic stress and depends on the chemical potential of ATP hydrolysis $\Delta\mu$; we refer the reader to [2] for a detailed derivation. In addition, $\zeta_{\alpha\beta}$ in general has an isotropic and an anisotropic part. The latter reflects local anisotropies in the material, such as filament ordering, which is characterized by a nematic-order parameter.

In this paper, we consider a thin shell made of an active elastic material, following the constitutive equation (1). A thin shell has negligible thickness compared to characteristic transverse-length scales, and is represented in a thin shell theory by a two-dimensional surface. To reduce the 3D equations for the deformation of the material in the shell to the 2D equations for the surface shape, assumptions on the deformations occurring in the thin shell cross-section are required. We follow the hypothesis of the Love–Kirchhoff theory: transverse normal stresses are negligible, and points on a straight line normal to the surface before deformation are on a straight line normal to the deformed surface after deformation [3]. Forces acting in the three-dimensional bulk of the shell give rise to tensions and moments acting on the two-dimensional shell cross-section. Equation (1) states that the stress within the shell material is the sum of an elastic and an active stress; therefore, the resulting tensions and moments can also be separated into elastic and active contributions. Passive elastic shells have been extensively studied [3, 4], and we focus here on the effects introduced by the active tensions and moments in the shell. Because these forces act internally in the bulk of the material, they generate

deformations that are different from those induced by external forces acting on the boundary of the shell.

In the last section of the paper, we apply this theory to describe cell deformations of adhering zebrafish embryo cells. We use image analysis to extract geometrical parameters characterizing the cell deformation. Using a fitting procedure to compare these measurements with theoretical deformation profiles, we extract the elastic and bending moduli of the cell cortex, which are key parameters of the cell mechanics. The strength of this method is that it allows for nonperturbative measurements, where information is obtained by analyzing the shapes of cells.

The paper is organized as follows. In section 1, force and torque balance equations are derived for an active elastic shell in the framework of differential geometry. These equations are then obtained in the special case of an axisymmetric surface. To gain insight into the effect of active terms, we consider the stability of a cylinder under internal tension and its response to a localized increase of active tensions or moments. In section 2, we apply this model to the analysis of the shape of three adhering cells and the cell deformation resulting from the disruption of the contact between two of the cells. We show that the predicted shapes obtained with the active shell theory reproduce experimental observations, and we extract from fits of experimental cell deformations a value for the cortex stretching modulus and cortex thickness.

2. Derivation of shell theory with active tensions and moments

2.1. Tensions, moments, and force and torque balance

We start by deriving constitutive equations for the tensions and moments within an active elastic shell, following the assumptions detailed in the introduction. We use notations from differential geometry, with lower indices denoting covariant coordinates and upper indices denoting contravariant coordinates. Indices can be raised or lowered by contraction with the surface metric tensor g defined in equation (A.2). We denote with indices (i, j) the coordinates on the shell surface and with greek letters (α, β, γ) the 3D coordinates. Partial derivatives are denoted ∂_i and covariant derivatives are denoted ∇_i. We consider a two-dimensional surface parametrized by two coordinates $\mathbf{X}(s^1, s^2)$ (figure 1(A)). The two local tangent vectors are denoted $\mathbf{e}_1$ and $\mathbf{e}_2$, the normal vector to the surface is $\mathbf{n}$, g_{ij} is the metric tensor, and C_{ij} is the curvature tensor (appendix A).

The surface is assumed to be subjected to internal tensions and moments. Considering a curve drawn on the surface $\mathbf{X}(s)$ with local tangent vector $\boldsymbol{\tau} = \partial_s \mathbf{X}(s)$ and normal vector $\boldsymbol{\nu} = \mathbf{n} \times \boldsymbol{\tau}$, the force $\mathbf{f}$ and torque $\boldsymbol{\Gamma}$ acting on a section of the curve in between s and $s + ds$ is related to the tension and moments t and $\mathbf{m}$ by

$$\mathbf{f} = ds\, \nu_i t^i, \qquad \boldsymbol{\Gamma} = ds\, \nu_i \mathbf{m}^i \tag{2}$$

with $ds|\boldsymbol{\nu}|$ the length of the section (figure 1(B)). Decomposing t^i and $\mathbf{m}^i$ in to tangential and normal components yields the definition of the tension and moment tensors

$$t^i = t^{ij}\mathbf{e}_j + t^i_n \mathbf{n}, \qquad \mathbf{m}^i = m^{ij}\mathbf{e}_j + m^i_n \mathbf{n} \tag{3}$$

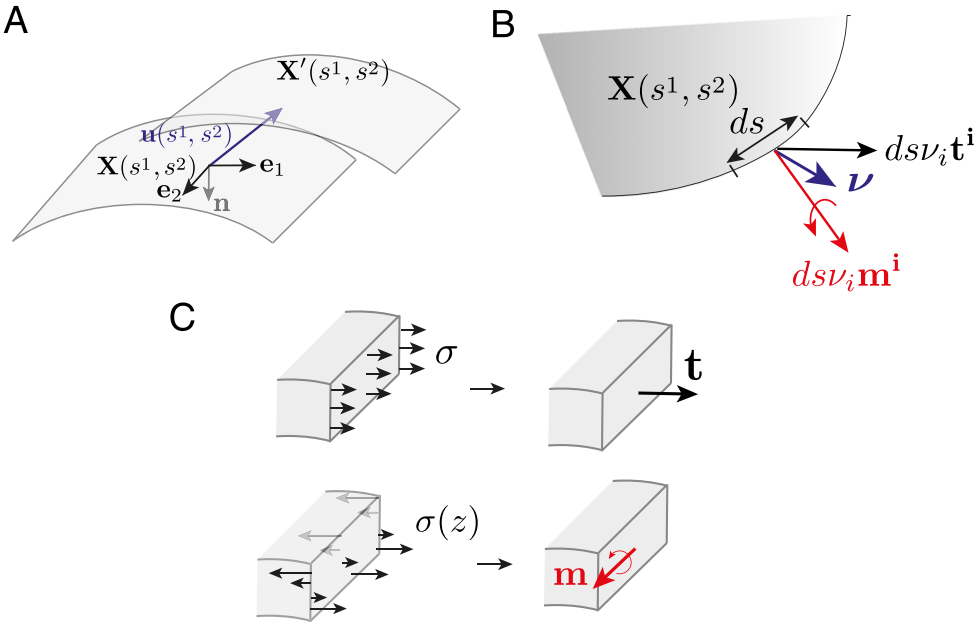

Figure 1. Notations for physical quantities associated with the elastic shell. (A) The shell is represented by a surface denoted by $\mathbf{X}(s^1, s^2)$, with tangent vectors $\mathbf{e}_1$, $\mathbf{e}_2$ and normal vector $\mathbf{n}$, deformed into a new surface $\mathbf{X}'(s^1, s^2) = \mathbf{X}(s^1, s^2) + \mathbf{u}(s^1, s^2)$. (B) Forces and moments acting in the shell: a tension tensor t and a moment tensor $\mathbf{m}$ are introduced such that the force acting on a segment of the shell with length ds normal to ν is given by $ds\nu_i t^i$, and the torque acting on the segment is given by $ds\nu_i\mathbf{m}^i$. (C) Schematic illustrating how stresses acting within the shell result in tensions and moments acting along the thin shell surface.

With these definitions, force balance on the surface $\mathbf{X}$ reads [5]

$$\nabla_i t^{ij} - C_i^j t_n^i = \sigma_{\text{out}}^{nj} - \sigma_{\text{in}}^{nj} \tag{4}$$

$$\nabla_i t_n^i + C_{ij} t^{ij} = \sigma_{\text{out}}^{nn} - \sigma_{\text{in}}^{nn} \tag{5}$$

$$\nabla_i m^{ij} - C_i^j m_n^i - \epsilon_i^{\ j} t_n^i = 0 \tag{6}$$

$$\nabla_i m_n^i + C_{ij} m^{ij} + \epsilon_{ij} t^{ij} = 0 \tag{7}$$

with ϵ_{ij} the Levi-Civita tensor defined such that $\epsilon_{11} = \epsilon_{22} = 0$ and $\epsilon_{12} = -\epsilon_{21} = \sqrt{g}$ (appendix A). These equations correspond, respectively, to force balance parallel and normal to the local plane tangent to the surface, and moment balance parallel and normal to the local tangent plane. $\boldsymbol{\sigma}_{\text{out}}^n$ and $\boldsymbol{\sigma}_{\text{in}}^n$ are the external stresses acting on the shell from the medium inside and outside the shell, and we assume that no external torque density acts on the surface. In this paper, we consider physical situations where $t_i^{\ j}$ is a symmetric tensor and where m_{ij} is the product of a symmetric tensor with the Levi-Civita tensor (appendix B).

We now consider a thin layer of material whose constitutive equation is given by equation (1), and derive the tensions and moments in the thin shell. We assume that the thin shell has a thickness h, and z denotes the transverse coordinate going across the z direction in the shell,

with $z = 0$ in the middle of the shell. Tensions and moments are obtained by integrating the force and torques acting on an infinitesimal cross-section of the shell of length ds and normal vector $\boldsymbol{\nu}$ (figure 1(C)):

$$t_i \nu^i = \int_{-\frac{h}{2}}^{\frac{h}{2}} dz\, \boldsymbol{\sigma}_i \nu^i(z), \quad \mathbf{m}_i \nu^i = \int_{-\frac{h}{2}}^{\frac{h}{2}} dz\, \mathbf{r} \times \boldsymbol{\sigma}_i \nu^i(z) \tag{8}$$

where $\mathbf{r}$ is a vector spanning the shell cross-section and $\boldsymbol{\nu}(z)$ is the local vector on the cross-section at position z, with $\boldsymbol{\nu}(0) = \boldsymbol{\nu}$.

Because the total stress acting inside the shell has contributions from the elastic and active stresses (equation (1)), the tensions and moments are also the sums of the elastic tensions and moments t_e and m_e and the active tensions and moments t_a and m_a:

$$t = t_\mathrm{e} + t_\mathrm{a} \tag{9}$$

$$m = m_\mathrm{e} + m_\mathrm{a}. \tag{10}$$

To obtain the expression of the elastic tensions and moments, $\mathbf{X}$ is defined to be the reference surface, i.e., the surface configuration in which elastic stresses exerted in the shell vanish. The elastic tensions and moments are then obtained by writing that the surface $\mathbf{X}$ is deformed to a new surface $\mathbf{X}' = \mathbf{X} + \mathbf{u}(s^1, s^2)$, where $\mathbf{u}$ is the vector of deformation of the shell (figure 1(A)). To first order in the deformation $\mathbf{u}$, the surface $\mathbf{X}'$ has a modified metric tensor $g'_{ij} \simeq g_{ij} + 2u_{ij}$, where $u_{ij} = \frac{1}{2}(\mathbf{e}_i \cdot \partial_j \mathbf{u} + \mathbf{e}_j \cdot \partial_i \mathbf{u})$ is the 2D strain of the surface $\mathbf{X}$, and a modified curvature tensor $C_i'^j \simeq C_i^j + c_i^j$. Note that c_i^j is defined as the difference of the curvature tensors in mixed coordinates, and in general, $C'_{ij} \neq C_{ij} + c_{ij}$.

To obtain the 3D strain of the shell from the expression of u_{ij} and c_{ij}, we follow the Love–Kirchhoff approximation for thin shells [3]: the surface $\mathbf{X}$ is defined to be the middle surface of the shell, points on normals of the initial surface lie on normals to the deformed surface after deformation, and the transverse normal stresses σ_{iz} are negligible, because the shell is in contact with a viscous fluid that, at steady state, is at rest. As a consequence, for thin shells, internal shear stresses acting parallel to the surface of the shell are small compared to internal stresses that compress or extend the mean surface [6].

With these assumptions, the 3D deformation in the shell is given by $\epsilon_{ij} = u_{ij} - z c_{ij}$. From this expression, the elastic tensions and moments can be obtained using the derivation detailed in appendix B:

$$t_{\mathrm{e}_{ij}} = 2S\Big(\big(1-\nu\big)u_{ij} + \nu u_k^k g_{ij}\Big) \tag{11}$$

$$m_{\mathrm{e}_{ij}} = -2B\Big(\big(1-\nu\big)c_i^k + \nu c_m^m \delta_i^k\Big)\epsilon_{kj} \tag{12}$$

with $S = \frac{Eh}{2(1-\nu^2)}$ the stretching modulus of the shell and $B = \frac{Eh^3}{24(1-\nu^2)}$ its bending modulus.

We now proceed to obtain the active contribution to tensions and moments t_a and m_a. These quantities will, in general, depend on the profile of active stress within the shell. We assume here that the shell is subjected to the active stress

$$\zeta_{\alpha\beta} = \zeta_\mathrm{a}(z)\big(\delta_{\alpha\beta} - n_\alpha n_\beta\big) \tag{13}$$

with n_α the components of the vector normal to the surface so that the active stress is assumed to act along the directions parallel to the shell, both in the reference and deformed configuration. In the cell cortex, such a stress distribution can be generated, for instance, by filaments oriented parallel to the surface of the cell [7]. $\zeta_a(z)$ is the active stress profile perpendicular to the midsurface of the shell. Tensions depend on the integral of the stress profile along the cross-section $\int dz\zeta_a(z)$, while moments depend on the integral $\int dzz\zeta_a(z)$. For simplicity, we assume here that the stress profile is linear within the shell, such that the active stress profile can be written $\zeta(z) \simeq \zeta_a(0) + z\partial_z\zeta_a\big|_{z=0}$. This expression can also be seen as an expansion to first order in z of the active stress profile. With this assumption, we obtain the following tension and moment tensors:

$$t_{a_{ij}} = t_a g_{ij} \tag{14}$$

$$m_{a_{ij}} = m_a \epsilon_{ij} \tag{15}$$

with $t_a = \zeta_a(0)h$ the resultant active tension across the shell and $m_a = \frac{h^3}{12}\partial_z\zeta_a\big|_{z=0}$ the resultant moment. Active tensions are, therefore, associated with average active stresses in the shell, while active moments are associated with variations of active stress across the height of the shell. With the earlier simplification, the active tension and moment tensors take a remarkably simple form, with the tension tensor being proportional to the metric and the moment tensor proportional to the Levi-Civita tensor, with $m_{a_{ij}}$ antisymmetric.

With the specification of boundary conditions, the equations for the shape of an elastic shell subjected to active tensions and moments can be obtained from the set of equations (4)–(7) and (11)–(14).

2.2. Axisymmetric active shell

2.2.1. General equations. We now turn to the case of an axisymmetric active shell. The shape of the surface is set by specifying the generating curve $(r(s), z(s))$, such that a point on the surface $\mathbf{X}(s, \phi)$ has the expression in the Cartesian basis $(\mathbf{e}_x, \mathbf{e}_y, \mathbf{e}_z)$:

$$\mathbf{X}(s, \phi) = r(s)\cos\phi\,\mathbf{e}_x + r(s)\sin\phi\,\mathbf{e}_y + z(s)\mathbf{e}_z \tag{16}$$

so that the surface shape is generated by rotation of the angle ϕ around the axis $\mathbf{e}_z$. The vectors tangential to the shape are given by $\mathbf{e}_s = \partial_s\mathbf{X}$ and $\mathbf{e}_\phi = \partial_\phi\mathbf{X}$, and the vector normal to the shape pointing inward is given by $\mathbf{n} = \frac{\mathbf{e}_s\times\mathbf{e}_\phi}{|\mathbf{e}_s\times\mathbf{e}_\phi|}$. The arc length s is chosen to be an Euclidean coordinate so that $|\mathbf{e}_s| = 1$. The angle formed by $\mathbf{e}_s$ with the plane normal to the z axis is denoted $\psi(s)$ (figure 2) and is related to r and z through $\partial_s r = \cos(\psi(s))$ and $\partial_s z = \sin(\psi(s))$. With these definitions, the metric and curvature tensors are given by

$$g_{ij} = \begin{pmatrix} 1 & 0 \\ 0 & r^2 \end{pmatrix}, \quad C_i^j = \begin{pmatrix} \partial_s\psi & 0 \\ 0 & \dfrac{\sin(\psi)}{r} \end{pmatrix}. \tag{17}$$

The deformation vector $\mathbf{u}$ has projections tangential and normal to the initial surface so that $\mathbf{u} = u^s(s)\mathbf{e}_s + u^n(s)\mathbf{n}$. The variations after deformation of the metric and curvature tensor read

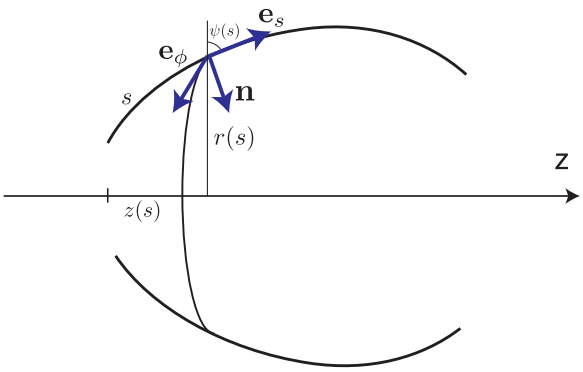

Figure 2. Geometrical quantities associated with the axisymmetric surface, with rotational symmetry around the axis z. s is a curvilinear coordinate, $r(s)$ is the distance of the shell from the z axis, and $\psi(s)$ is the angle between the local tangent vector $\mathbf{e}_s$ and the vertical axis.

$$u_i^{\ j} = \begin{pmatrix} \partial_s u^s - \partial_s\psi\, u^n & 0 \\ 0 & \dfrac{\cos\psi\, u^s - \sin\psi\, u^n}{r} \end{pmatrix} \tag{18}$$

$$c_i^{\ j} = \begin{pmatrix} \partial_s^2 u^n + \partial_s\psi\partial_s u^s + \partial_s^2\psi\, u^s - \partial_s\psi\, u_s^{\ s} & 0 \\ 0 & \dfrac{\cos\psi}{r}\left(\partial_s\psi\, u^s + \partial_s u^n\right) - \dfrac{\sin\psi}{r}u_\phi^{\ \phi} \end{pmatrix}. \tag{19}$$

Following equation (11), the tangential elastic tensions and moments are given by

$$t_{ei}^{\ \ j} = 2S\begin{pmatrix} u_s^{\ s} + \nu u_\phi^{\ \phi} & 0 \\ 0 & \nu u_s^{\ s} + u_\phi^{\ \phi} \end{pmatrix} \tag{20}$$

$$m_{ei}^{\ \ j} = 2Br\begin{pmatrix} 0 & -\left[c_s^{\ s} + \nu c_\phi^{\ \phi}\right] \\ \nu c_s^{\ s} + c_\phi^{\ \phi} & 0 \end{pmatrix} \tag{21}$$

and the active tensions and moments are given by

$$t_{ai}^{\ \ j} = t_a\begin{pmatrix} 1 & 0 \\ 0 & 1 \end{pmatrix} \tag{22}$$

$$m_{aij} = m_a r\begin{pmatrix} 0 & 1 \\ -1 & 0 \end{pmatrix}. \tag{23}$$

In the previous expression, m_a has the dimension of a torque per unit length; the components of m_{aij}, however (as well as the components of $m_{ai}^{\ \ j}$ and $m_a^{\ ij}$), do not necessarily have dimension of a torque per unit length because cylindrical coordinates are not Euclidean.

2.2.2. Deformations away from an undeformed state under homogeneous active tension. We assume that the shell has a reference state with no elastic stress, but is subjected to an uniform active tension t_a. Such a state would be reached in the long time limit for a viscoelastic fluid

subjected to active stress. We also assume that the shell is in contact with a fluid exerting a uniform pressure P_{in} and P_{out}, respectively, inside and outside the shell. The shell equilibrium equation in the undeformed state then reads:

$$\left(\partial_s\psi + \frac{\sin\psi}{r}\right)t_{\text{a}} = \Delta P \tag{24}$$

which is the law of Laplace for an axisymmetric surface, with $\frac{1}{2}\left(\partial_s\psi + \frac{\sin\psi}{r}\right)$ the mean curvature of the axisymmetric surface. The shapes satisfying this equation are, therefore, Delaunay surfaces, i.e., surfaces of revolutions with constant mean curvature [8].

A perturbation of this initial shape, whether from a change in boundary conditions, a change in the pressure of the surrounding fluid $\Delta P' = \Delta P + \delta P$, a small isotropic change in the active tension $t_{\text{as}}{}^{s} = t_{\text{a}} + \delta t_{\text{a}}$, $t_{a\phi}{}^{\phi} = t_{\text{a}} + \delta t_{\text{a}}$, or in the active moment $m_{\text{as}\phi} = r\,(m_{\text{a}} + \delta m_{\text{a}})$ and $m_{\text{a}\phi s} = -r\,(m_{\text{a}} + \delta m_{\text{a}})$, can all lead to a deformation of the surface. A local modification of the active stress could be caused, for instance, by a change in the concentration of molecular motors giving rise to active stresses [7, 9]. The force balance in equations (4)–(6) can then be rewritten for the total stress $t = t_{\text{e}} + t_{\text{a}}$ (ignoring the normal moment balance equation, which is automatically satisfied for the axisymmetric shell):

$$\nabla'_i t_{\text{e}}^{ij} - C'_i{}^{j} t_n^i = -\nabla'_i t_{\text{a}}^{ij} \tag{25}$$

$$\nabla'_i t_n^i + C'_{ij} t_{\text{e}}^{ij} = \Delta P' - C'_{ij} t_{\text{a}}^{ij} \tag{26}$$

$$\nabla'_i m_{\text{e}}^{ij} - t_n^j = -\nabla'_i m_{\text{a}}^{ij} \tag{27}$$

where the metric g', curvature tensor C' and covariant derivatives ∇' are now taken on the deformed surface and are, therefore, functions of the initial surface shape defined by $r(s)$, $z(s)$, as well as the deformation $\mathbf{u}$. We only consider here small deformations, and equations (25)–(27) can, therefore, be expanded to linear order in the deformation. For the axisymmetric case, these equations read

$$\partial_s t_{\text{es}}{}^{s} + \frac{\cos\psi}{r}\left(t_{es}{}^{s} - t_{\text{e}\phi}{}^{\phi}\right) - \partial_s\psi t_n^s = -\partial_s\delta t_{\text{a}} \tag{28}$$

$$\partial_s t_n^s + \frac{\cos\psi}{r}t_n^s + \partial_s\psi t_{\text{es}}{}^{s} + \frac{\sin\psi}{r}t_{\text{e}\phi}{}^{\phi} = \delta P - t_{\text{a}}\left(c_s^s + c_\phi^\phi\right) - \left(\partial_s\psi + \frac{\sin\psi}{r}\right)\delta t_{\text{a}} \tag{29}$$

$$\partial_s m_{\text{es}}{}^{\phi} + \frac{\cos\psi}{r}\left(2m_{\text{es}}^{\phi} + \frac{m_{\text{es}}^{\phi}}{r^2}\right) - \frac{1}{r}t_n^s = -\frac{\partial_s\delta m_{\text{a}}}{r} \tag{30}$$

and equation (7) identically vanishes. This system can be reduced to a system of two equations by eliminating t_n^s between equation (29) and (30). Expliciting the elastic tensions and moments from equations (20) and (21) then gives rise to a differential equation of the form

$$a_0u_s + a_1\partial_s u_s + a_2\partial_s^2 u_s + b_0u_n + b_1\partial_s u_n + b_2\partial_s^2 u_n + b_3\partial_s^3 u_n = -\partial_s\delta t_{\text{a}} + \partial_s\psi\delta m_{\text{a}} \tag{31}$$

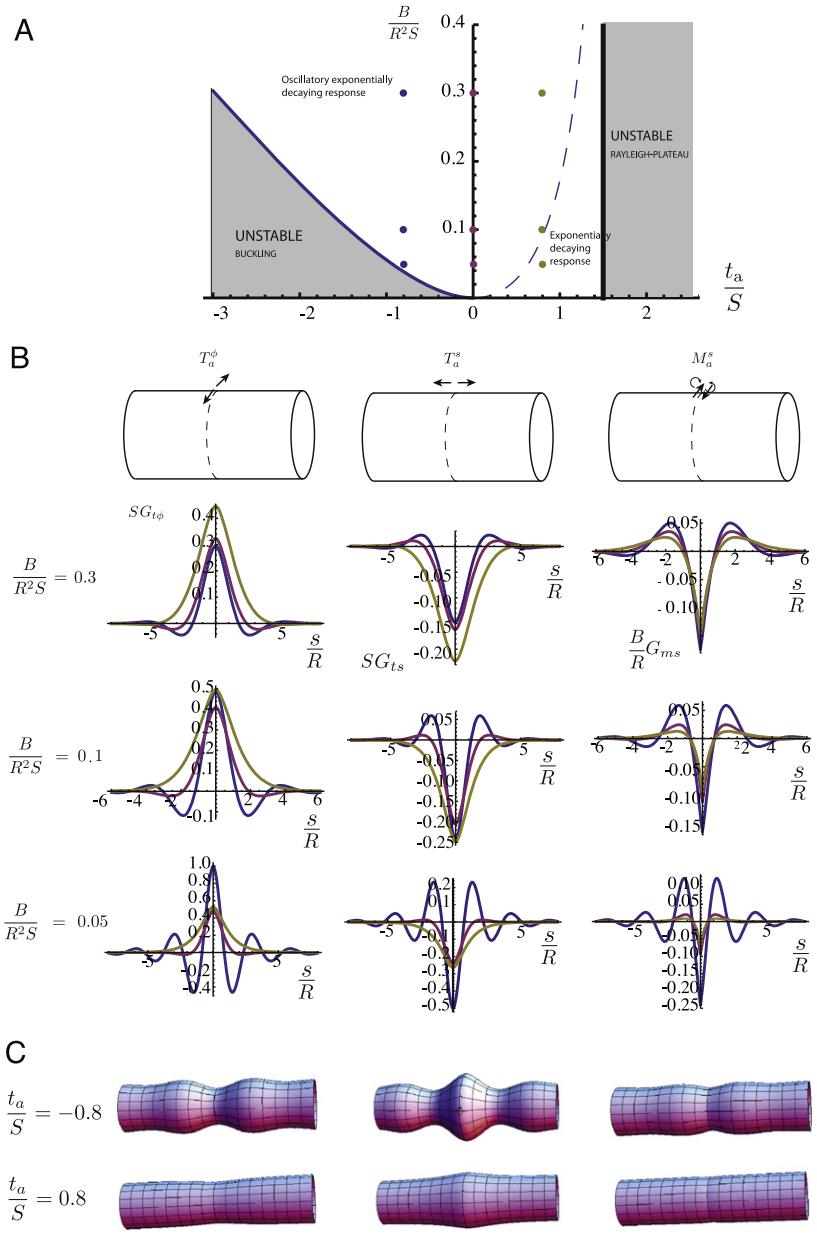

Figure 3. (A) Stability diagram of an infinite elastic cylinder with surface tension t_a for the Poisson ratio $\nu = \frac{1}{2}$. For large positive tension $t_a > \frac{3S}{2}$, the cylinder undergoes a Plateau–Rayleigh instability, while for large negative tension, a buckling instability at finite wavelength occurs. (B) The Green functions G_{ts}, $G_{t\phi}$ and G_{ms} give the radial deformation u_n induced by a localized increase in active tension t_a^{ϕ}, t_a^{s} or active moment m_a^{s}. With the conventions used in this paper, a positive deformation u_n corresponds to a deformation oriented inside the cylinder. The colored curves correspond to different values of $\frac{t_a}{S}$ (blue: $\frac{t_a}{S} = -0.8$, red: $\frac{t_a}{S} = 0$, yellow: $\frac{t_a}{S} = 0.8$). (C) 3D representation of the cylinder deformation induced by a localized increase of active tension or moments. Shapes are obtained for $\frac{B}{R^2S} = 0.05$ and, respectively, $\frac{T_a^{\phi}}{RS} = 0.5$, $\frac{T_a^{s}}{RS} = 0.5$, $\frac{M_a^{s}}{B} = 0.5$. The cylinder is represented for $-4 < \frac{s}{R} < 4$.

$$c_0 u_s + c_1 \partial_s u_s + c_2 \partial_s^2 u_s + c_3 \partial_s^3 u_s + d_0 u_n + d_1 \partial_s u_n + d_2 \partial_s^2 u_n + d_3 \partial_s^3 u_n + d_4 \partial_s^4 u_n$$
$$= \delta P - t_a \left(c_s^s + c_\phi^\phi \right) - \left(\partial_s \psi + \frac{\sin \psi}{r} \right) \delta t_a - \left(\partial_s^2 + \frac{\cos \psi}{r} \partial_s \right) \delta m_a \tag{32}$$

where the coefficients a_i, b_i, c_i and d_i are given in appendix E. One can verify that equations (31) and (32) have total order 6 and their resolution, therefore, requires us to specify six integration constants. By specifying the moments and forces on the shell boundary, six additional conditions can, in principle, be obtained; the requirement that the total force acting on the shell be zero removes one of these boundary conditions, leaving us effectively with five boundary conditions. Eliminating deformations corresponding to a pure translation of the shape removes one additional integration constant, allowing us to solve for the deformed shape.

2.3. Green function for the deformation of a cylinder

To gain physical insight into equations (28)–(30), we now consider the stability and response to a perturbation of an infinite elastic cylindrical shell. An undeformed infinite cylindrical shell is under equilibrium for a uniform distribution of active tension t_a and active moment m_a, but the equilibrium can be unstable. The stability phase diagram of the shell is plotted in figure 3. The shell stability depends on the active tension t_a, but not on the active moment m_a. For large positive active tension $t_a > 2(1 - \nu^2)S$, an instability occurs at large wavelengths, for $q \to 0$. This instability is related to the Plateau–Rayleigh instability caused by surface tension in fluids [10], and its threshold does not depend on the bending modulus B, so that an infinitely long stable cylinder with positive active tension t_a is stable only for a large enough elastic modulus of the shell. For a sufficiently large negative tension, on the other hand ($t_a < 0$), a buckling instability occurs at the critical compressive threshold for buckling of a cylindrical elastic shell; for small bending modulus, the instability occurs for an active tension $t_a < -2\sqrt{\frac{3BS}{R^2}}$. Therefore, the cylindrical shape is stable only for intermediate values of the active tension t_a. The diagram we obtain has similarities with the stability diagram of [11], where the elasticity of a substrate surrounding the shell plays the role of the shell-stretching elastic modulus introduced here.

We now consider the deformation of an infinite cylindrical shell triggered by a perturbation in active tension or active moment in the stable region of the diagram. Because the equations for the deformations are linear, this procedure allows us to compute the Green function, giving the shell deformation induced by a local point force. Considering a perturbation occurring either in the directions s or ϕ:

$$t_{ai}{}^{j} = \begin{pmatrix} t_a + \delta t_a^s & 0 \\ 0 & t_a + \delta t_a^\phi \end{pmatrix} \quad m_{a_{ij}} = R \begin{pmatrix} 0 & \delta m_a^s \\ -\delta m_a^\phi & 0 \end{pmatrix}, \tag{33}$$

we wish to obtain the radial and tangential deformations in the form

$$u_n(s) = \int_{-\infty}^{+\infty} ds' \Big[G_{ts}\left(s - s'\right)\delta t_{\mathrm{a}}^{s}\left(s'\right) + G_{t\phi}\left(s - s'\right)\delta t_{\mathrm{a}}^{\phi}\left(s'\right) + G_{ms}\left(s - s'\right)\delta m_{\mathrm{a}}^{s}\left(s'\right) + G_{m\phi}\left(s - s'\right)\delta m_{\mathrm{a}}^{\phi}\left(s'\right)\Big]. \tag{34}$$

Using equations (31)–(32), one can compute the four corresponding Green functions (see appendix D). One finds that $G_{m\phi} = 0$: perturbations in the moment acting perpendicularly to the cylinder do not induce deformations because of the cylindrical symmetry. The other Green functions are decreasing exponentially with $|s - s'|$ for all types of perturbations over a characteristic length, which depends on t_{a}, S, and B. For small tension t_{a}, the deformation decays with a length scaling as $\sqrt{hR}$, whereas for large tension, it decays with a length proportional to $R\sqrt{\frac{t_{\mathrm{a}}}{2(1-\nu^2)S - t_{\mathrm{a}}}}$, which diverges when the shell becomes unstable to a Plateau–Rayleigh instability (appendix D).

The magnitude of the perturbation depends on the nature of the perturbation applied. As one might expect, an increase in the azimuthal tension t_{a}^{ϕ} induces a radial constriction of the cylinder. An increased tension along the axis of the cylinder t_{a}^{s}, however, induces a compression in the plane and a radial expansion of the shape (figure 3). In the limit of small bending modulus $B/S \ll R^2$ and small active tension $t_{\mathrm{a}} \ll S$, both deformations are of order $u_n \sim w\sqrt{R/h}\,\delta t_{\mathrm{a}}/S$, with w the width on which the perturbation is applied and δt_{a} its magnitude.

A local increase in active moment induces a deformation in the cylinder oriented toward the outside of the cylinder when $m_{\mathrm{a}}^{s} > 0$ ($u_n < 0$); as pointed out earlier, such a moment can be generated by an asymmetric distribution of stress across the shell, with higher stresses toward the inside of the shell. The maximum amplitude of the deformation scales as $u_n \sim R\sqrt{\frac{h}{R}}\frac{\delta m_{\mathrm{a}} w}{B}$, with δm_{a} the magnitude of the perturbation.

To compare perturbations induced by changes in active tension and active moments, one can consider the deformation induced by a perturbation of the active stress profile $\delta\zeta_a(z)$, with mean across the shell $\langle\delta\zeta_{\mathrm{a}}\rangle$ and variation across the shell $\sim\Delta\delta\zeta_{\mathrm{a}}$. Such a perturbation results in a variation of active tension $\delta t_{\mathrm{a}} = h\langle\delta\zeta_{\mathrm{a}}\rangle$ and active moment $\delta m_{\mathrm{a}} = \Delta\delta\zeta_{\mathrm{a}}h^2$. The deformation arising from the mean active stress scales like $u_n \sim \sqrt{Rh}\frac{w\delta\zeta_{\mathrm{a}}}{S}$, while the deformation arising from the variation of active stress scales like $u_n \sim \sqrt{Rh}\frac{\Delta\delta\zeta_{\mathrm{a}} w}{S}$. Therefore, the ratio of deformations scales like $\Delta\delta\zeta_{\mathrm{a}}/\delta\zeta_{\mathrm{a}}$ and active moments have to be taken into account when the variation of active stress across the shell becomes comparable to the mean active stress.

3. Active shell theory applied to cell shape changes upon cell–cell contact disruption

In this section, the theory of active axisymmetric shells is applied to the analysis of experiments performed on zebrafish germ-layer progenitors [13]. Progenitors of the three distinct germ layers—ectoderm, mesoderm, and endoderm—form during gastrulation, a developmental process that is conserved among most animals. The formation of distinct layers is thought to rely on the ability of cells to form cell–cell contacts, which depend on cells' contractile and

adhesive properties [12, 14]. Using a dual micropipette aspiration assay [15, 16], we have previously studied the adhesive properties of zebrafish germ-layer progenitors [13]. We use here a similar experimental setup and investigate cell shape changes during the mechanical separation of a cell-cell contact. In a cell-triplet assay, three ectoderm progenitors are brought into contact to form a linear aggregate (figure 5(A) and appendix G). Within five minutes of contact time, the cell shapes and the contact regions reach a stationary size. The two cells on the outside of the cell triplets (side cells) are aspirated into two micropipettes, which are positioned such that the cell triplet is kept under tension (figure 4(A)). One of the two micropipettes is then pulled away with a velocity of 20 μm s^{-1}, such that one of the side cells is detached from the cell triplet. Within 10 s after detachment, the former contact zone of the middle cell forms a bulge reaching a steady-state configuration for about one minute (figure 4(B)). The bulge results from the decrease in cortical tension in the adhesion zone following contact formation: consistent with this, cortical actin and myosin concentrations are reduced at the contact [1]. To study the mechanical properties of zebrafish progenitor cells, we decided to apply our theoretical model to describe the cell shape reached after detachment. We show here that the active shell theory accounts well for the middle cell deformation following detachment of the side cell. Comparison of theory with measurements of the cell shape further allows us to extract key cellular mechanical parameters characterizing the active tension and cell elasticity.

Precise analysis of overall cell shape is difficult in these experiments because isolated zebrafish progenitors display continuous blebbing at their surface (figure 5(A)). Instead, a few key geometrical parameters characterizing the shape of cell doublets and cell triplets were extracted from experiments (figure 4). Two frames per experiment are used for geometrical measurements: the first one just before the pipette is pulled is used to characterize the shape of the three adhering cells, and the second frame, after cell detachment and once the bulge has reached its maximum size, is used to characterize the shape of the bulging cell. Table 1 reports the mean and standard deviation from measurements on $N = 10$ experiments.

More specifically, we analyzed the cell shape before and after detachment as follows:

1. Before cell detachment, the cell triplet is considered to be symmetric with respect to the vertical plane going through the center of the middle cell, and the initial shapes of the three cells are characterized by the angles formed by the cell interfaces at their junction θ_s, θ_i, and $\psi(s_i) = \pi - \psi(s_f)$; the radii of the cell contact r_i; and the volume V of the central cell (table 1). The mean volume V is determined by measuring the volume of spherical cells before they are brought into contact.

To describe cell shape before detachment, we assume that all cortical elastic stresses vanish, since the cell shape is allowed to relax on a timescale longer than the typical actin cortex viscoelastic timescale, which is expected to be smaller than a minute [1]. The cell interfaces are, therefore, assumed to be under active homogeneous tension γ_s, γ_i and t_a (figure 4(A)). Because the side cells are aspirated in micropipettes, we assume that their surface tension γ_s can differ from the surface tension of the central cell t_a. Under these assumptions, the interfaces of the side cells are portions of a sphere, while the middle cell surface is a surface of constant mean curvature whose shape satisfies equation (24). Using experimental measurements of the cell volume V, contact angle $\psi(s_i)$, and side contact radius r_i (table 1) and solving the shape of equation (24) for the middle cell, we find a cell shape in good agreement with experimental

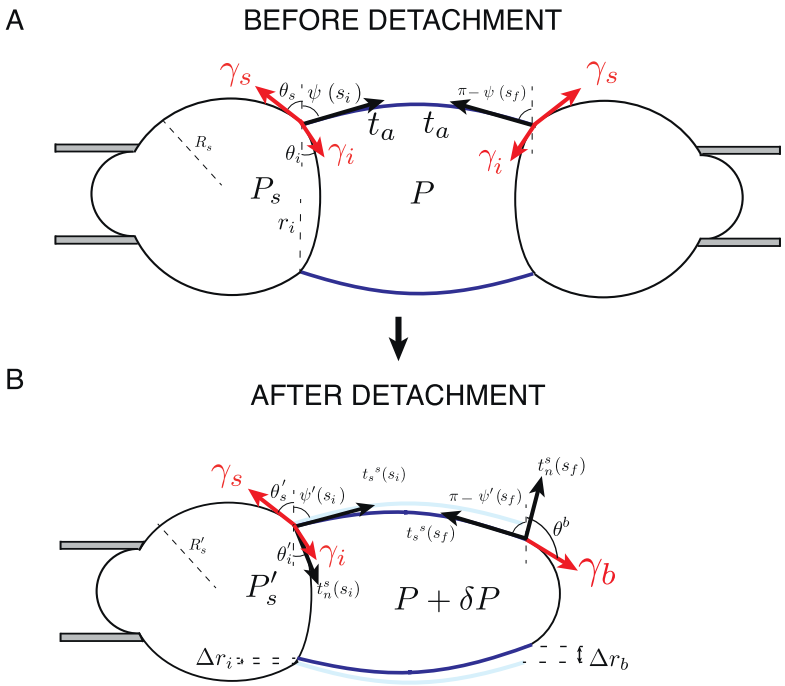

Figure 4. Schematic of the cell detachment experiment and hypothesis of the physical description. In the experiment, three cells are put together with micropipette manipulation and left to adhere. The cell on the right is detached from the cell triplet using a micropipette, leading the former contact zone to bulge out of the cell. (A) Before deformation, all interfaces are considered to have a surface tension arising from active processes in the cortex. (B) After deformation, the cortex in the body of the middle cell (blue thick line) is described as an active elastic shell, while the bulge region and remaining interface, having a less dense actin cortex, are considered surfaces with homogeneous tension. Red arrows: forces exerted on the actin cortex of the middle cell body by the surrounding interfaces. Black arrows: forces exerted by the middle cell body cortical shell on the surrounding interfaces.

observations for an end-to-end contour length $L = 22.4 \pm 1\,\mu$m and a mean curvature $C = 0.089 \pm 0.001\,\mu\text{m}^{-1}$. By then writing the force balance equations at the boundaries between the middle cell and the side cell, we obtain two additional equations:

$$t_a - \gamma_i \cos(\theta_i + \psi(s_i)) + \gamma_s \cos(\theta_s + \psi(s_i)) = 0 \tag{35}$$

$$-\gamma_s \sin(\theta_s + \psi(s_i)) + \gamma_i \sin(\theta_i + \psi(s_i)) = 0. \tag{36}$$

By solving the4se two equations for known angles θ_i, θ_s and $\psi(s_i)$, a value for the tensions γ_s/t_a and γ_i/t_a can be obtained (table 2). We find that both γ_s and γ_i have values larger than the middle cell cortical tension t_a. Micropipette aspirations of the two side cells may indeed result in an increase in their surface tension, possibly due to the corresponding increase in cell surface area.

2. After detachment of one of the side cells, the bulge grows and reaches a maximum size, which is stationary for about one minute, after which the bulge retracts and the middle cell adopts a spherical shape. The geometry of the middle cell cortex is quantified for the maximum bulge size. The updated angles θ_s', $\psi'(s_i)$, θ_i' and $\psi'(s_f)$, were measured, as well

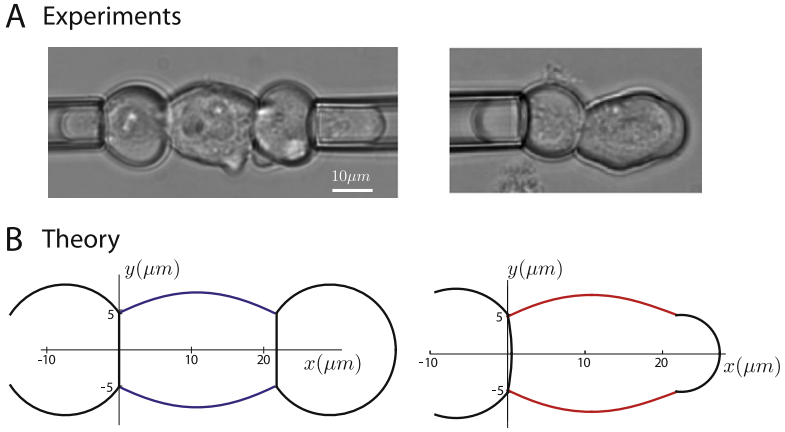

Figure 5. Experimental and theoretical cell deformation before and after cell detachment. The theoretical cell shape is calculated using parameters obtained from a fit to experimental measurements of cell deformation. (A) Cell triplet visualized with transmission microscopy before and after cell detachment. (B) Initial and final shapes of the cell triplet obtained using active elastic shell theory. The initial shape of the middle cell body is obtained by solving equation (24). The two side cells have spherical cap shapes. The interfaces are flat. The final shape of the middle cell body is obtained by solving equations (28)–(30) with boundary conditions given in equations (38)–(45). The side cell, interface, and bulge have a spherical cap shape. The values of geometrical parameters used to determine these shapes are given in tables 1 and 2.

Table 1. Measurement for the cell shape before (upper table) and after (lower table) deformation (see figure 4 for the parameters, definitions). Uncertainties are standard deviation.

V (μm^3)	θ_s	θ_i	$\psi(s_i) = \pi - \psi(s_f)$	r_i (μm)		
3316± 360	0.60 ± 0.07	$\simeq 0$	1.14 ± 0.15	5.1 ± 0.58		
θ_s'	θ_i'	$\psi'(s_i)$	$\psi'(s_f)$	Δr_b (μm)	Δr_i (μm)	θ_b
0.65 ± 0.10	0.21 ± 0.11	1.07 ± 0.19	1.90 ± 0.31	–0.18 ± 0.67	–0.05 ± 0.18	1.44 ± 0.16

as the radial deformation of the point joining the body of the middle cell with the contact regions Δr_b and Δr_i (table 1). The volume variation in the middle cell body ΔV was measured from the volume enclosed in the bulge minus the volume of the spherical cap interface. These values are reported in table 1.

Because the region of the bulge has a reduced cortex and takes a spherical shape after bulging, we neglect elastic stresses in this region and describe the bulge as surfaces under a homogeneous tension. We assume that such a description also applies to the aspirated side cell and its interface with the middle cell, with the same surface tensions as before detachment. With these assumptions, the cell pressure P' and surface tension in the bulge γ_b can be readily obtained from the cell shapes' measurements. For simplicity, we set here the pressure of the fluid outside the cell P_0 to be a pressure of reference, and other pressures are expressed relative to P_0. The pressure in the side cell is equal to $P_s' = 2\gamma_s/R_s$ and by applying the law of Laplace to

Table 2. Parameter values extracted by fitting the theoretical deformations obtained from the active shell theory to the experimental measurements. Uncertainties are standard deviations.

L (μm)	C (μm^{-1})	γ_s/t_a	γ_i/t_a	γ_b/t_a	S/t_a	B/t_a (μm^2)
22.4 ± 1	0.089 ± 0.003	1.61 ± 0.28	1.74 ± 0.43	0.59 ± 0.92	27.1 ± 3.5	7.7 ± 1.1

the interface in between the two remaining cells, the pressure after detachment in the middle cell is $P' = P'_s - 2\gamma_i/R_i$. Assuming that the pressure is balanced between the body of the middle cell and the bulge, one obtains the pressure in the middle cell $P' = 2\gamma_b/R_b$ from the law of Laplace applied to the bulge. From these two relations, one obtains the pressure balance relation

$$\frac{2\gamma_b}{R_b} = \frac{2\gamma_s}{R_s} - \frac{2\gamma_i}{R_i}. \tag{37}$$

By measuring R_i, R_b and R_s and using the values of γ_s/t_a and γ_i/t_a previously estimated, an evaluation of the ratio of tension of the bulge to the active tension in the cell can be obtained: $\gamma_b/t_a = 0.59 \pm 0.92$, indicating that the cortical tension in the contact zone is reduced.

The region of the middle cell outside of the bulge and the remaining contact zone, called thereafter the middle cell body, is described by an active shell theory with vanishing active moments. A membrane theory alone could not account for the observed cell shape, as the shape at the transition between the middle cell body and the bulge is not continuous. It is, therefore, necessary to take into account bending moments and to introduce a normal stress t_n^s acting across the shell to balance the external forces. We assume that the cell shape before detachment has no elastic stress and is, therefore, the reference shape of the middle cell cortex.

To reproduce the shape observed experimentally, equations (28)–(30) are solved with a multiple shooting method [18]. Boundary conditions are specified by assuming that no external torque is applied on the middle cell body, and that forces are balanced between the middle cell and the contacting areas:

$$t_{es}^{\ s}(s_i) + t_a - \gamma_i \cos(\theta_i + \psi'(s_i)) + \gamma_s \cos(\theta_s + \psi'(s_i)) = 0 \tag{38}$$

$$t_n^s(s_i) - \gamma_s \sin(\theta_s + \psi'(s_i)) + \gamma_i \sin(\theta_i + \psi'(s_i)) = 0 \tag{39}$$

$$m_s^{\phi}(s_i) = 0 \tag{40}$$

$$t_n^s(s_f) + \gamma_b \sin(\psi'(s_f) - \theta_b) = 0 \tag{41}$$

$$m_s^{\phi}(s_f) = 0 \tag{42}$$

where the three first equations apply on the side of the remaining cell and the two last equations on the bulge side. Note that the tangential force balance on the bulge

$$t_{es}^{\ s}(s_f) + t_a - \gamma_b \cos(\psi'(s_f) - \theta_b) = 0 \tag{43}$$

is not included, as it is automatically implied from equation (38) and conservation of the total force acting on a plane perpendicular to the symmetry axis. Because the solution is invariant by translation, one can further impose without loss of generality that the shell point in contact with the remaining cell does not move along the z direction:

$$u^n(s_i)\cos\psi(s_i) + u^s(s_i)\sin\psi(s_i) = 0. \tag{44}$$

Finally, cell volume conservation imposes that the variation of the volume δV enclosed by the shell,

$$\delta V = \int_{s_i}^{s_f} ds\pi\left(r'^2\sin\psi' - r^2\sin\psi\right) \tag{45}$$

$$= \pi\int_{s_i}^{s_f} dsr^2\sin\psi\left(2\frac{u^s}{r}\cos\psi - 2\frac{u^n}{r}\sin\psi + \partial_s u^s - \partial_s\psi\, u^n + \cot\psi\partial_s u^n + \cot\psi\partial_s\psi\, u^s\right) \tag{46}$$

obeys $\delta V = -\Delta V$, with ΔV the sum of two contributions to volume change: one from the volume enclosed by the bulge, and the other from the volume change due to the shape change of the undetached contact area.

From the boundary conditions and the shape before deformation, a solution for the cell shape can then be obtained by setting S/t_a, B/t_a, γ_s/t_a, γ_i/t_a, γ_b/t_a and the cell volume V, and introducing values of θ_s', θ_i', θ_b in the boundary conditions (38)–(42). As previously described, the ratio γ_s/t_a, γ_i/t_a, and γ_b/t_a, the angles $(\theta_s', \theta_i', \theta_b)$, and the cell volume V are extracted from the analysis of the shape before and after deformation. There are, therefore, two free parameters $(S/t_a, B/t_a)$ that can be adjusted to fit the remaining experimental measurements. To perform this fitting procedure, we define an objective function $\mathcal{S}$:

$$\begin{aligned}\mathcal{S}\left(\frac{S}{t_a}, \frac{B}{t_a}\right) = &\left((\Delta r_b^n - \Delta r_b^e)/\delta_{\Delta rb}\right)^2 + \left((\Delta r_i^n - \Delta r_i^e)/\delta_{ri}\right)^2 \\ &+ \left((\Delta\cos\psi'^n(s_i) - \Delta\cos\psi'^e(s_i))/\delta_{\Delta\cos\psi'(s_i)}\right)^2 \\ &+ \left((\Delta\cos\psi'^n(s_f) - \Delta\cos\psi'^e(s_f))/\delta_{\Delta\cos\psi'(s_i)}\right)^2 \\ &+ \left(\left(P'^n - P'^e\right)/\delta_{\Delta P}\right)^2\end{aligned} \tag{47}$$

evaluating the distance between geometrical quantities characterizing the shape obtained numerically and the shape observed experimentally, as well as the cellular pressure after deformation. The parameters with the e superscript correspond to measured data, the variables with the n superscript are numerical results and depend on $(S/t_a, B/t_a)$. The difference between the experimental value and the numerical result $(X^n - X^e)$ is weighted by the experimental standard deviation of X, δ_X. The normalized intracellular pressure difference P'^e/t_a between the initial and final shape is obtained as follows: in the initial configuration, the law of Laplace imposes $P_i'^e/t_a = 2C$, where C is the mean curvature of the middle cell surface. In the final configuration, the intracellular pressure is assumed to be balanced in the cell, and the pressure P_f^e in the middle cell is taken to be equal to the pressure in the bulge $P_f'^e/t_a = 2\gamma_b/t_a R_b$. Numerical minimization of the objective function $\mathcal{S}$ yields $S/t_a = 27.1 \pm 1.1$ and $B/t_a = 7.7 \pm 0.34\ \mu\text{m}^2$ (uncertainties are standard error of the mean with $N = 10$ cells; see appendix F for details). To compare the outcome of the fitting procedure with experiments, we plot in figure 5(B) the theoretical cell shape obtained for $S/t_a = 27.1$ and $B/t_a = 7.7\,\mu\text{m}^2$. The deformation field

(u^n, u^s) and tensions and moments corresponding to the final shape of the middle cell body are given in figure 6.

4. Discussion

The mechanics and deformations of thin elastic plates and shells have been extensively studied [3, 4, 19–21]. Recently, elastic shell theories have been used to describe the shape of biological objects, such as the faceting of viruses [22] or the folding of pollen grains [23]. Within the classical theory of shells, the elastic surface minimizes energy dependent on the magnitude of the deformations. Motivated by the description of the shape of biological systems that are working out of equilibrium by using the energy provided by ATP hydrolysis, we are interested here in describing active shells, taking into account the passive energetic cost of deformations, but also internal active processes, such that the equilibrium shell configurations do not necessarily minimize an energy. We have shown in this paper that active tensions and moments arise in the shell as a consequence of the distribution of active internal stress inside the shell. When the gradient of active stress across the shell becomes comparable to the mean value of the active stress, active moments in the shell have to be taken into account.

At the cell surface, the actomyosin cortex is subjected to stresses arising from myosin activity and other active processes. Precise regulation of these active stresses in space and time drives most shape changes [24]. For fast deformations, elastic stresses arise within the actin network [1]. The active elastic shell theory presented here therefore provides a valuable framework to describe short-timescale, cortex-driven cell deformations. The formation of cell membrane blebs following laser ablation of the actomyosin cortex in a rounded cell has been described by representing the cell surface as an elastic shell with active tension [25]. We show in this paper that the cell deformation following separation of adhering zebrafish embryo cells can also be understood within the framework of the active shell theory. From the analysis of the deformation, we have obtained values for the stretching and bending moduli of the cortex, normalized to the active tension of the cortex. From the ratio of bending to elastic moduli, we find a prediction for the cortex thickness of around 1.8 μm. This value is within the order of magnitude of reported values for cortex thickness, although larger values were reported for Hela and L929 cells [1, 26]. From measurements by atomic force microscopy (AFM) indentation of the surface tension of zebrafish embryonic cells ($t_a = 66 \pm 21$ pN μm^{-1} [27]) we can also obtain a corresponding 3D elastic bulk modulus $E/(1-\nu^2) = 1900 \pm 600$ Pa whose order of magnitude is in agreement with previous measurements [25, 28]. Besides, the length $\sqrt{B/S}$ gives an estimate of the range of the deformation induced by a local force, which we find to be of the order of 0.53 μm. Note that for the sake of simplicity, we have assumed here that active moments within the cortex can be neglected. It is unclear, however, whether such active moments are significant in the actomyosin cell cortex. Possibly, an inhomogeneous distribution of myosin concentration across the thickness of the actin cortex generates active moments. So far, current imaging resolution has not allowed us to resolve such a profile across the cortex thickness. Future experiments will have to investigate the consequences of active moments on cell mechanics.

A proper control of cellular mechanics is essential for cell and tissue morphogenesis [24, 29]. An important bottleneck in the quantitative investigation of cell mechanics is the scarcity of experimental methods for measuring cellular physical properties. Properties like

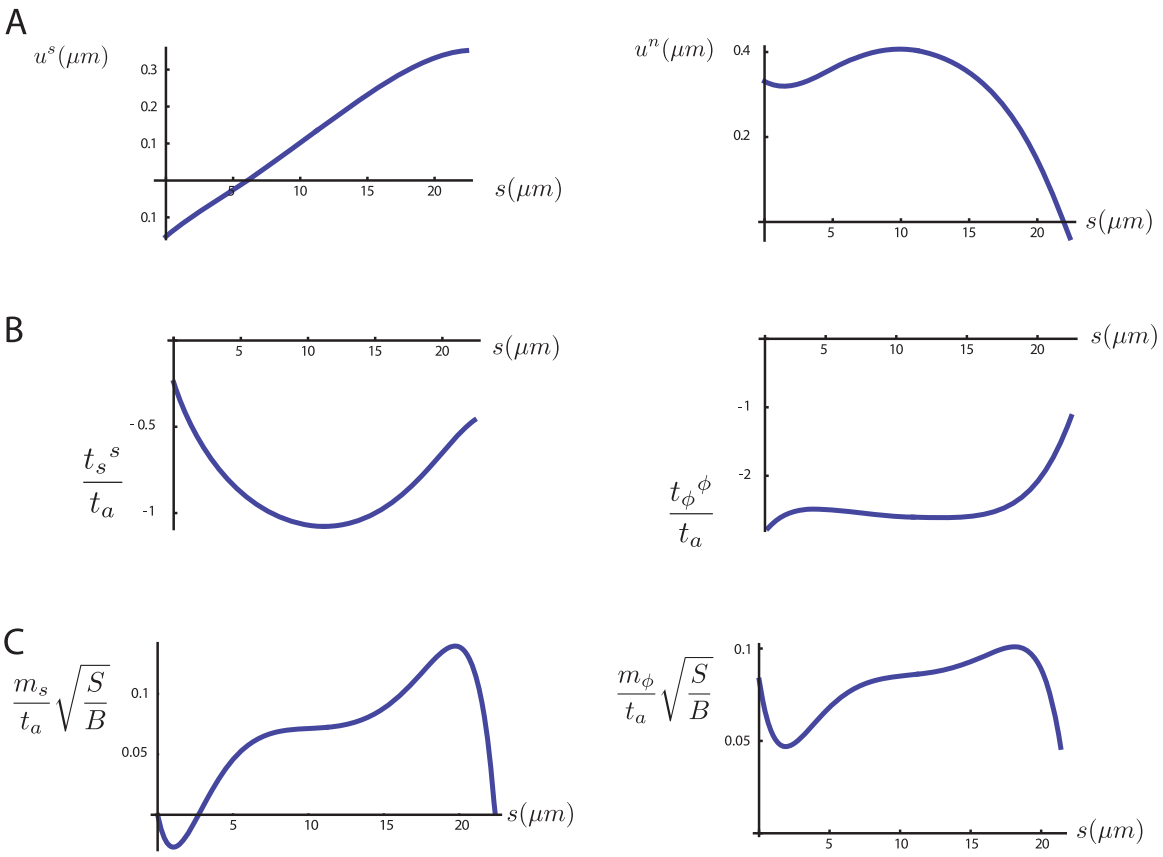

Figure 6. Deformation field, elastic tensions and moments along the middle cell body. (A) Tangential and normal contributions of the deformation field as functions of the arc length s. The functions $(u^n(s), u^s(s))$ are obtained by solving equations (28)–(30) with boundary conditions given in equations (38)–(45). (B) Rescaled elastic tensions as functions of the arc length s. The functions $t_s^s(s)$ and $t_\phi^\phi(s)$ are obtained from the deformation field using equation (20). (C) Rescaled elastic moments as functions of the arc length s. The functions $m_s(s) = r(s)\, m_s^\phi(s)$ and $m_\phi = -m_\phi^s(s)/r(s)$ are obtained from the deformation field using equation (21). The results are obtained for $(S/t_a = 27.1,\ B/t_a = 7.7\,\mu\text{m}^2)$ and using the geometrical parameters given in tables 1 and 2.

cortex tension and elasticity are typically assessed by micropipette aspiration, atomic force microscopy indentation or laser ablation; all of these techniques require direct cell manipulation and are thus difficult to perform *in vivo*. The theory presented here provides a less pertubative way to measure the mechanical properties of the cortex of adhering cells, based on a precise analysis of cell shape changes upon detachment. The measurement relies on image analysis alone. The theory presented here can thus serve as a starting point for the development of new imaging-based approaches to investigate the mechanics of cells during cortex-driven rapid cell shape changes *in vivo*, including bleb formation [30] and epithelial contractions [31].

The formalism introduced here could also help understand the deformations of epithelia during development. In epithelial cells, an actomyosin cytoskeleton is present at the apical and basal surfaces of the cell, generating active stresses [32, 33]. Apicobasal polarity could give rise to differences in actomyosin concentration across the cell height, leading to an inhomogeneous

distribution of active stresses and, therefore, to active moments acting across the tissue. Apical constriction, i.e., overactivation of myosin contractility solely on the apical side of epithelial cells, has, for instance, been associated with tissue bending in *Drosophila* gastrulation, groove formation at segment boundaries, or formation of the morphogenetic furrow in eye disc development [34–37]. In these examples, patterning by genes results in protein activation modifying the cellular generation of stress in specific regions of the tissue. In physical terms, regions of increased internal tensions and moments drive deformations of the epithelial surface. As detailed in section 2.3, the resulting amplitude and length scale of the deformation will depend on the inherent mechanical properties of the tissue as well as on the magnitude of the perturbation.

More generally, cells and tissue can establish a given shape by regulating the spatial distribution of active tensions and moments. The Green functions introduced in section 2.3 connect the shape of a thin layer of material to the distribution of stresses generated within it. Inversion of these Green functions could be used to recover the pattern of stress generated in a biological shell from its shape, provided that the mechanical parameters of the shell are known. Furthermore, our calculation of the Green functions predicts the range and shape of the deformation profile induced by a local increase of active tension or moment. This prediction could be tested through experiments, allowing us to rapidly increase myosin activity at specific locations on the cell surface. We have here limited our calculation to deformations of shells perturbed axisymmetrically; it would be interesting to obtain the response to any spatial distribution of local perturbation of the active stress and torque.

In this work, active effects have been included by adding an active stress contribution to the elastic stress (equation (1)). An alternative choice could be to impose an active strain. A decomposition of the deformation gradient into a growth-induced part and an elastic part has been proposed in [38–40] to model growth of 2D elastic tissues. It has been shown within this framework that anisotropic growth can induce structures like curling and crumpling that are observed in plants.

Finally, although the equations in this paper have been written for an elastic material, it would be interesting to express similar equations for a material with fluid properties within the surface. This requires us to keep track of the flow field within the plane, as well as the surface deformation out of the plane. Constitutive equations can be obtained by replacing the material deformation u with a velocity vector v and the elastic modulus E with a viscosity η. The surface shape then evolves according to the equation $d\mathbf{X}/dt = \mathbf{v}$. The expression of force balance, however, will depend not only on velocities, but also on the out-of-plane surface deformation u^n. Such a fluid description would be suited to describe the long-time behavior of the shape of the cell surface. Performing detachment experiments at different speeds could allow us to explore the transition between viscous and elastic behaviour of the cortex. Such a complete description could then be applied to analyze shape changes in processes involving deformations on multiple timescales, such as cell division and cell motility. It will be interesting to investigate the effect of active moments in this limit.

Appendix A. Notations of differential geometry and force balance

In this appendix, we give definitions of differential geometries used in the text. We consider a two-dimensional surface parameterized by two coordinates $\mathbf{X}(s^1, s^2)$. Two tangent vectors and a normal vector are associated with every point on the surface, according to

$$\mathbf{e}_1 = \frac{\partial \mathbf{X}}{\partial s^1}, \quad \mathbf{e}_2 = \frac{\partial \mathbf{X}}{\partial s^2}, \quad \mathbf{n} = \frac{\mathbf{e}_1 \times \mathbf{e}_2}{|\mathbf{e}_1 \times \mathbf{e}_2|}. \tag{A.1}$$

The metric g_{ij} and curvature tensor C_i^j associated with $\mathbf{X}$ are defined by

$$g_{ij} = \mathbf{e}_i . \mathbf{e}_j, \quad \partial_i \mathbf{n} = -C_i^j \mathbf{e}_j \tag{A.2}$$

and the derivatives of the basis vectors are given by

$$\partial_i \mathbf{e}_j = C_{ij}\mathbf{n} + \Gamma_{ij}^k \mathbf{e}_k \tag{A.3}$$

where the Christoffel coefficients Γ_{ij}^k are obtained from the metric by

$$\Gamma_{ij}^k = \frac{1}{2} g^{km} \Big[\partial_j g_{im} + \partial_i g_{jm} - \partial_m g_{ij} \Big]. \tag{A.4}$$

The surface area element is denoted $\sqrt{g}\, ds^1 ds^2$, where $g = \det(g_{ij})$ is the determinant of the metric.

The Levi-Civita antisymmetric tensor has the following definition:

$$\epsilon_{ij} = \sqrt{g} \begin{pmatrix} 0 & 1 \\ -1 & 0 \end{pmatrix}, \quad \epsilon^{ij} = \frac{1}{\sqrt{g}} \begin{pmatrix} 0 & 1 \\ -1 & 0 \end{pmatrix} \tag{A.5}$$

and it satisfies the identity

$$\epsilon_{ij}\epsilon^{jk} = -\delta_i^k. \tag{A.6}$$

The Levi-Civita tensor is useful to express vectorial products of the basis vectors:

$$\mathbf{n} \times \mathbf{e}_i = \epsilon_i^j \mathbf{e}_j \tag{A.7}$$

$$\mathbf{e}_i \times \mathbf{e}_j = \epsilon_{ij}\mathbf{n}. \tag{A.8}$$

We denote ∂_i partial derivatives and ∇_i covariant derivative, defined for a vector v^i or a tensor t^{ij}, by

$$\nabla_i v^j = \partial_i v^j + \Gamma_{ik}^j v^k \tag{A.9}$$

$$\nabla_i t^{jk} = \partial_i t^{jk} + \Gamma_{il}^j t^{lk} + \Gamma_{il}^k t^{jl}. \tag{A.10}$$

The projection of a 3D tensor $T_{\alpha\beta}$ on the surface $\mathbf{X}$ defines a surface tensor T_{ij}, such that:

$$T_{ij} = T_{\alpha\beta} \mathbf{e}_i^\alpha \mathbf{e}_j^\beta \tag{A.11}$$

where the contraction with coordinates α and β is performed with the metric of the 3D space.

Finally, force balance of tensions and moments on the surface takes the form [5]

$$\nabla_i t^i = \boldsymbol{\sigma}_{\text{out}}^n - \boldsymbol{\sigma}_{\text{in}}^n \tag{A.12}$$

$$\nabla_i \mathbf{m}^i = t^i \times \mathbf{e}_i \tag{A.13}$$

where the stress in the surrounding medium inside the surface $\boldsymbol{\sigma}_{\text{in}}$ induces a stress $\boldsymbol{\sigma}_{\text{in}}^n = n_\alpha \boldsymbol{\sigma}_{\text{in}}^\alpha$ on the surface and the stress outside the surface $\boldsymbol{\sigma}_{\text{out}}$ induces a stress $\boldsymbol{\sigma}_{\text{out}}^n = n_\alpha \boldsymbol{\sigma}_{\text{out}}^\alpha$ on the surface, with the convention that $\mathbf{n}$ is pointing inside the surface. We consider here furthermore that no external torque acts on the surface. Using the decomposition of the external stress

$$\boldsymbol{\sigma}^{n}_{\text{out}} = \sigma^{ni}_{\text{out}}\mathbf{e}_i + \sigma^{nn}_{\text{out}}\mathbf{n} \tag{A.14}$$

$$\boldsymbol{\sigma}^{n}_{\text{in}} = \sigma^{ni}_{\text{in}}\mathbf{e}_i + \sigma^{nn}_{\text{in}}\mathbf{n} \tag{A.15}$$

together with the definitions of the tangential tensions and moments in the surface (equation (3)) yield the force balance equation (4–7).

Appendix B. Calculation of tensions and moments acting on the shell

We derive next the constitutive equations for tensions and moments in a thin shell subjected to an arbitrary stress distribution in the surface $\sigma^{(0)}_{\alpha\beta} + z\sigma^{(1)}_{\alpha\beta}$ (the higher order of the expansion of the stress in z is neglected). Using the definition in equation (A.11), we consider the result on a shell cross-section of the projection of the stress on the surface $\sigma^{(0)}_{ij} + z\sigma^{(1)}_{ij}$. Other transverse components of the stress are assumed to be negligible. We consider a curve drawn on the surface $\mathbf{X}(s)$ with local tangent vector $\boldsymbol{\tau} = \partial_s\mathbf{X}(s)$ and normal vector $\boldsymbol{\nu} = \mathbf{n} \times \boldsymbol{\tau}$ (figure B1). Considering a cross-section element of the shell spanned by a curvilinear coordinate $-\frac{\Delta s}{2} < ds < \frac{\Delta s}{2}$, calculations are done to the lowest order in the length Δs and in the shell thickness h. One can then derive the metric associated with the surface defined by this cross-section element. Denoting $\mathbf{O}$ the center of the cross-section, a point $\mathbf{M}$ on the cross section is denoted by its coordinates $-\frac{\Delta s}{2} < ds < \frac{\Delta s}{2}$ and $-\frac{h}{2} < z < \frac{h}{2}$, according to

$$\mathbf{OM} = ds\boldsymbol{\tau} + z\mathbf{n} = ds^1\mathbf{e}_1 + ds^2\mathbf{e}_2 + z\mathbf{n} \tag{B.1}$$

with $ds^i/ds = \tau^i$. The two tangent vectors and normal vector to the cross-section element in $\mathbf{M}$ are then given by:

$$\boldsymbol{\tau}(z) = \partial_s\mathbf{OM} = \boldsymbol{\tau} - z\tau^i C_i^j\mathbf{e}_j \tag{B.2}$$

$$\partial_z\mathbf{OM} = \mathbf{n} \tag{B.3}$$

$$\boldsymbol{\nu}(z) = \mathbf{n} \times \boldsymbol{\tau}(z) = \boldsymbol{\nu} - z\tau^i C_i^j \epsilon_j^k \mathbf{e}_k = \boldsymbol{\nu} + z\epsilon_l^i \nu^l C_i^j \epsilon_j^k \mathbf{e}_k. \tag{B.4}$$

Using these relations, one can obtain force and torques acting on the cross-section arising from the stress σ and relate them to the tension and bending moments acting on the shell. The force on the segment is given by

$$\mathbf{f} = \Delta s\nu^i t_i^j \mathbf{e}_j = \Delta s \int_{-h/2}^{h/2} dz\nu^i \sigma_i^j \mathbf{e}_j \tag{B.5}$$

where the first equality arises from the definition of the tension tensor (equation (2)) and the second equality is obtained by a direct calculation of the force to the lowest order in h. Identification then yields the expression for the tension tensor.

$$t_{ij} = \int_{-h/2}^{h/2} dz\sigma_{ij} \simeq h\sigma^{(0)}_{ij}. \tag{B.6}$$

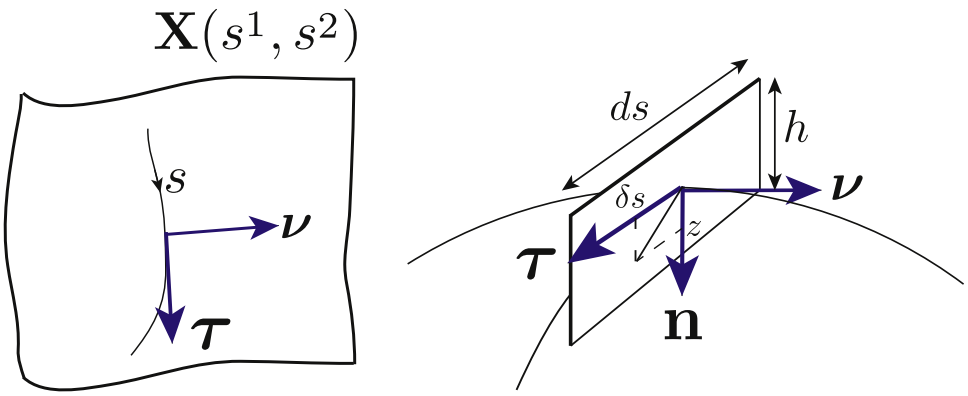

Figure B1. Notations for the calculations of forces and torques on a segment of the shell. Tensions and moments are obtained by integrating forces and torques on a shell cross-section.

The torque acting on the segment is

$$\begin{aligned}\boldsymbol{\Gamma} &= \Delta s \nu^i m_i{}^j \mathbf{e}_j = \Delta s \int_{-h/2}^{h/2} dz z \mathbf{n} \times \left(\nu^i(z) \left(\sigma^{(0)}{}_i{}^j + z \sigma^{(1)}{}_i{}^j \right) \mathbf{e}_j \right) \\ &= \Delta s \int_{-h/2}^{h/2} dz z \left(\nu^i + z \epsilon_k^l \nu^k C_l^m \epsilon_m^i \right) \left(\sigma^{(0)}{}_i{}^j + z \sigma^{(1)}{}_i{}^j \right) \epsilon_j^l \mathbf{e}_l \\ &\simeq \nu^i \Delta s \left[\int_{-h/2}^{h/2} dz z^2 \sigma^{(1)}{}_i{}^k + \int_{-h/2}^{h/2} dz z^2 \epsilon_i^p C_p^m \epsilon_m^l \sigma^{(0)}{}_l{}^k \right] \epsilon_k^j \mathbf{e}_j \end{aligned} \tag{B.7}$$

where the first equality arises from the definition of the moment tensor (equation (2)) and the second equality is obtained by evaluating the torque on the cross-section and further expanding in lower order in z and h. Identification then yields the expression for the moment tensor

$$m_{ij} = \frac{h^3}{12} \left[\sigma_{ik}^{(1)} + \epsilon_i^m C_m^l \epsilon_l^p \sigma_{pk}^{(0)} \right] \epsilon_j^k . \tag{B.8}$$

The second term in equation (B.7) can be neglected in the force balance equation compared to higher-order terms arising from the tension tensor. Therefore, we ignore it in the expressions given in the text. From the expression for the tensions and moment tensor in equations (B.6) and (B.7) and the expression for the elastic and active stresses in equations (1) and (13), one obtains the values for the tensions and bending moments due to elastic stress and active internal stresses given in equations (11), (12) and (14).

Appendix C. Deformation tensor in Love–Kirchoff theory

In this appendix, we justify the expression for the symmetric deformation tensor within the Love–Kirchoff approximation, $a_{ij} = u_{ij} - z c_{ij}$. Following deformation of the shell and within the Love–Kirchoff approximation, a point initially located within the shell on $\tilde{\mathbf{X}}(s^1, s^2, z) = \mathbf{X}(s^1, s^2) + z\mathbf{n}$ ends up in the new shell on location $\tilde{\mathbf{X}}'(s^1, s^2, z) = \mathbf{X}'(s^1, s^2) + z\mathbf{n}'$, with $\mathbf{n}'$ the normal to the deformed surface $\mathbf{X}'$. Two points infinitesimally close within the shell are then separated by a vector, before and after deformation, respectively:

$$\mathbf{dx} = (ds^i - z ds^j C^i_j)\mathbf{e}_i + dz\mathbf{n} \tag{C.1}$$

$$\mathbf{dx}' = (ds^i - z ds^j C'^i_j)\mathbf{e}'_i + dz\mathbf{n}' \tag{C.2}$$

with $\mathbf{e}'_i = \partial_i \mathbf{X}' = \mathbf{e}_i + \partial_i \mathbf{u}$ and $C'^{ij}_i = -\partial_i \mathbf{n}' . \mathbf{e}_j$. Eliminating the infinitesimal displacements ds^i, dz between equations (C.1) and (C.2), expanding to lower order in z, and neglecting the transverse deformations $\partial_i \mathbf{u} \cdot \mathbf{n}$ allows us to write the deformed vector $\mathbf{dx}'$ as a function of the original vector $\mathbf{dx}$:

$$\mathbf{dx}' \simeq \mathbf{dx} \cdot \mathbf{e}^i \left[\delta_i^{\ j} - z(C'^{ij}_i - C^j_i) + (\partial_i \mathbf{u}) \cdot \mathbf{e}^j \right] \mathbf{e}_j + (\mathbf{dx} \cdot \mathbf{n})\mathbf{n}. \tag{C.3}$$

Thus, within the approximations shown here the tangential part of the material deformation tensor F defined by $dx'^j = F^j_i dx^i$ has the expression

$$F^j_i = \delta_i^{\ j} - z c_i^{\ j} + (\partial_i \mathbf{u}) \cdot \mathbf{e}^j \tag{C.4}$$

and the symmetric deformation gradient tensor $a_{ij} = \frac{1}{2}(F_{ij} + F_{ji}) - g_{ij}$ is given by $a_{ij} = u_{ij} - z c_{ij}$.

Appendix D. Green functions for the deformation of a cylinder

In this appendix, we derive expressions for the Green functions introduced in equation (34), giving the deformation of a cylinder as a function of a perturbation in active tension or active moment. We consider a cylinder of radius R, subjected to uniform active tension t_a, in equilibrium with a fluid with pressure in the cylinder P_{in} and pressure outside the cylinder P_{out}, such that the law of Laplace imposes $P_{in} - P_{out} = t_a/R$. A perturbation of active stresses and torques applied to the cylinder results in a deformation that we now compute. For a cylinder, $r(s) = R$, $z(s) = s$ and $\psi(s) = \frac{\pi}{2}$, and the force balance equations (28)–(30) can be combined with the expression for the tensions and moments (20), (21) and (33) to yield the following equation for the normal deformation

$$-2BR\partial_s^4 u_n + \left(Rt_a - \frac{2\nu B}{R} \right) \partial_s^2 u_n + \frac{t_a + 2S(\nu^2 - 1)}{R} u_n = \nu \delta t^s_a - \delta t^\phi_a - R\partial_s^2 \delta m^s_a \tag{D.1}$$

where it was assumed that the pressure difference across the shell does not vary, so that $\delta P = 0$, and the external tension acting on the shell boundaries is also constant. A change of active moment δm^ϕ_a does not induce deformations in the cylinder. Introducing the Fourier transform $\tilde{u}_n = \int u_n e^{-iqs} ds$, $\tilde{\delta t}^s_a = \int \delta t^s_a e^{-iqs} ds$, $\tilde{\delta t}^\phi_a = \int \delta t^\phi_a e^{-iqs} ds$, $\tilde{\delta m}^s_a = \int \delta m^s_a e^{-iqs} ds$ and the reduced variables $g = \frac{t_a}{S}$ and $b = \frac{B}{SR^2}$ ($b = \frac{h^2}{12}$ from the definitions of B and S in the main text), the equation for the radial deformation u_n takes the form in Fourier space:

$$\frac{\tilde{u}_n}{R} = G_1(q) \frac{\tilde{\delta t}^\phi_a - \nu \tilde{\delta t}^s_a}{S} + G_2(q) \frac{R \tilde{\delta m}^s_a}{B} \tag{D.2}$$

with

$$G_1(q) = \frac{1}{2b(Rq)^4 + (g - 2\nu b)(Rq)^2 + \left(2\left(1 - \nu^2\right) - g\right)} \tag{D.3}$$

$$G_2(q) = \frac{-b(Rq)^2}{2b(Rq)^4 + (g - 2\nu b)(Rq)^2 + \left(2\left(1 - \nu^2\right) - g\right)}. \tag{D.4}$$

When the denominator of $G_1(q)$ and $G_2(q)$ is negative for a range of positive values of q, the cylindrical shape is unstable. This occurs in two different regions:

- For large positive active tension $g > 2(1 - \nu^2)$, an instability occurs for $q \to 0$. This instability is related to the Plateau–Rayleigh instability caused by surface tension in fluids [10].
- For negative active tension $g < 0$ and $(g - 2b\nu)^2 - 8b\,(2 - g - 2\nu^2) > 0$, a buckling instability occurs at the critical compressive threshold for buckling of a cylindrical elastic shell [4]. For $b \to 0$, the instability threshold occurs for $g < -4\sqrt{1 - \nu^2}\sqrt{b}$ ($t_a < -4\sqrt{(1 - \nu^2)BS/R^2}$) and at the finite wavelength $\lambda = 2\pi\sqrt{R}\,(B/S(1 - \nu^2))^{\frac{1}{4}}$.

We now consider the deformation induced by a localized increase in active tensions and moments in the stable region of the diagram. We write $\delta t_{\rm a}^s = T_{\rm a}^s \delta(s)$, $\delta t_{\rm a}^\phi = T_{\rm a}^\phi \delta(s)$ and $\delta m_{\rm a}^s = M_{\rm a}^s \delta(s)$, with $T_{\rm a}^s$ and $T_{\rm a}^\phi$ two line tensions and $M_{\rm a}^s$ has the dimension of a torque. The corresponding deformations can be obtained by inverse Fourier transform of the functions $G_1(q)$ and $G_2(q)$:

$$\frac{u_n}{R} = G_1(s)\frac{T_{\rm a}^\phi - \nu T_{\rm a}^s}{RS} + G_2(s)\frac{M_{\rm a}^s}{B} \tag{D.5}$$

with $G_1(s)$ and $G_2(s)$ given by the following expressions:

- For $\left(g - 2b\nu\right)^2 - 8b\left(2 - g - 2\nu^2\right) < 0$

$$\begin{aligned} G_1(s) &= \frac{e^{-\alpha_2\frac{s}{R}}}{8b\alpha_1\alpha_2\left(\alpha_1^2 + \alpha_2^2\right)}\left[\alpha_1 \cos\frac{s\alpha_1}{R} + \alpha_2 \sin\frac{s\alpha_1}{R}\right]\Theta(s) \\ &\quad + \frac{e^{\alpha_2\frac{s}{R}}}{8b\alpha_1\alpha_2\left(\alpha_1^2 + \alpha_2^2\right)}\left[\alpha_1 \cos\frac{s\alpha_1}{R} - \alpha_2 \sin\frac{s\alpha_1}{R}\right]\Theta(-s) \end{aligned} \tag{D.6}$$

$$\begin{aligned} G_2(s) &= \frac{e^{-\alpha_2\frac{s}{R}}}{8\alpha_1\alpha_2}\left[-\alpha_1 \cos\frac{s\alpha_1}{R} + \alpha_2 \sin\frac{s\alpha_1}{R}\right]\Theta(s) \\ &\quad + \frac{e^{\alpha_2\frac{s}{R}}}{8\alpha_1\alpha_2}\left[-\alpha_1 \cos\frac{s\alpha_1}{R} - \alpha_2 \sin\frac{s\alpha_1}{R}\right]\Theta(-s). \end{aligned} \tag{D.7}$$

The coefficients α_1 and α_2 have lengthy expressions. In the limit $g \to 0$ and $b \to 0$, they are

given by $\alpha_1 \simeq \frac{(1-\nu^2)^{\frac{1}{4}}}{\sqrt{2}b^{\frac{1}{4}}} - \frac{g}{8\sqrt{2}(1-\nu^2)^{\frac{1}{4}}b^{\frac{3}{4}}}$ and $\alpha_2 \simeq \frac{(1-\nu^2)^{\frac{1}{4}}}{\sqrt{2}b^{\frac{1}{4}}} + \frac{g}{8\sqrt{2}(1-\nu^2)^{\frac{1}{4}}b^{\frac{3}{4}}}$. As the threshold for buckling is reached, $\alpha_2 \to 0$ and the length scale on which a deformation is induced diverges.

- For $(g-2b\nu)^2 - 8b\left(2-g-2\nu^2\right) > 0$, the deformation is decaying as a double exponential:

$$\begin{aligned} G_1(s) &= \frac{1}{4b\left(\alpha_3^2-\alpha_4^2\right)}\left[-\frac{1}{\alpha_3}e^{-\frac{s}{R}\alpha_3}+\frac{1}{\alpha_4}e^{-\frac{s}{R}\alpha_4}\right]\Theta(s) \\ &\quad + \frac{1}{4b\left(\alpha_3^2-\alpha_4^2\right)}\left[-\frac{1}{\alpha_3}e^{\frac{s}{R}\alpha_3}+\frac{1}{\alpha_4}e^{\frac{s}{R}\alpha_4}\right]\Theta(-s) \end{aligned} \tag{D.8}$$

$$\begin{aligned} G_2(s) &= \frac{1}{4\left(\alpha_3^2-\alpha_4^2\right)}\left[-\alpha_3 e^{-\frac{s}{R}\alpha_3}+\alpha_4 e^{-\frac{s}{R}\alpha_4}\right]\Theta(s) \\ &\quad + \frac{1}{4\left(\alpha_3^2-\alpha_4^2\right)}\left[-\alpha_3 e^{\frac{s}{R}\alpha_3}+\alpha_4 e^{\frac{s}{R}\alpha_4}\right]\Theta(-s). \end{aligned} \tag{D.9}$$

The coefficients α_3 and α_4 have lengthy expressions with $\alpha_3 > \alpha_4$, which in the limit $b \to 0$ reduce to $\alpha_3 \simeq \sqrt{\frac{g}{2b}}$ and $\alpha_4 \simeq \sqrt{\frac{2(1-\nu^2)-g}{g}}$, corresponding to decay lengths $\sqrt{\frac{2B}{t_a}}$ and $R^2\sqrt{\frac{t_a}{2(1-\nu^2)S-t_a}}$. As the unstable region $g \to 2(1-\nu^2)$ is approached, $\alpha_4 \to 0$ and the length scale on which a deformation is induced diverge as $R/\sqrt{2(1-\nu^2)-g}$.

Overall, for small tension t_a the functions G_1 and G_2 decrease exponentially with a decay length $\lambda \sim 2\pi R b^{\frac{1}{4}} \sim 2\pi\sqrt{hR}$, whereas for a large enough tension t_a they decrease as double exponentials, with the largest decay length $\lambda \sim R\sqrt{\frac{t_a/S}{2(1-\nu^2)-t_a/S}}$ (figure D1(B)). Therefore, different regions of tension t_a/S display different responses to perturbation.

The maximum values of the functions G_1 and G_2 are plotted in figure D1(A). They are given in the limit $b \to 0$, $g \to 0$ by $G_1(0) \simeq \frac{1}{4\sqrt{2}(1-\nu^2)^{\frac{3}{4}}b^{\frac{1}{4}}} - \frac{g}{32\sqrt{2}b^{\frac{3}{4}}(1-\nu^2)^{\frac{5}{4}}}$ and $G_2(0) = -\left[\frac{b^{\frac{1}{4}}}{4\sqrt{2}(1-\nu^2)^{\frac{1}{4}}} - \frac{g}{32\sqrt{2}b^{\frac{1}{4}}(1-\nu^2)^{\frac{3}{4}}}\right]$. As one might expect,for small tension, higher internal tension g leads to a smaller magnitude of the response (negative sign in front of g); this is not always the case, however, as for high tension, an increase in active tension t_a leads to a larger response to a perturbation in t_a^s or t_a^ϕ (figure D1).

The Green functions introduced in equation (34) are then related to G_1 and G_2 by

$$G_{ts}(s) = -\frac{\nu G_1(s)}{S} \tag{D.10}$$

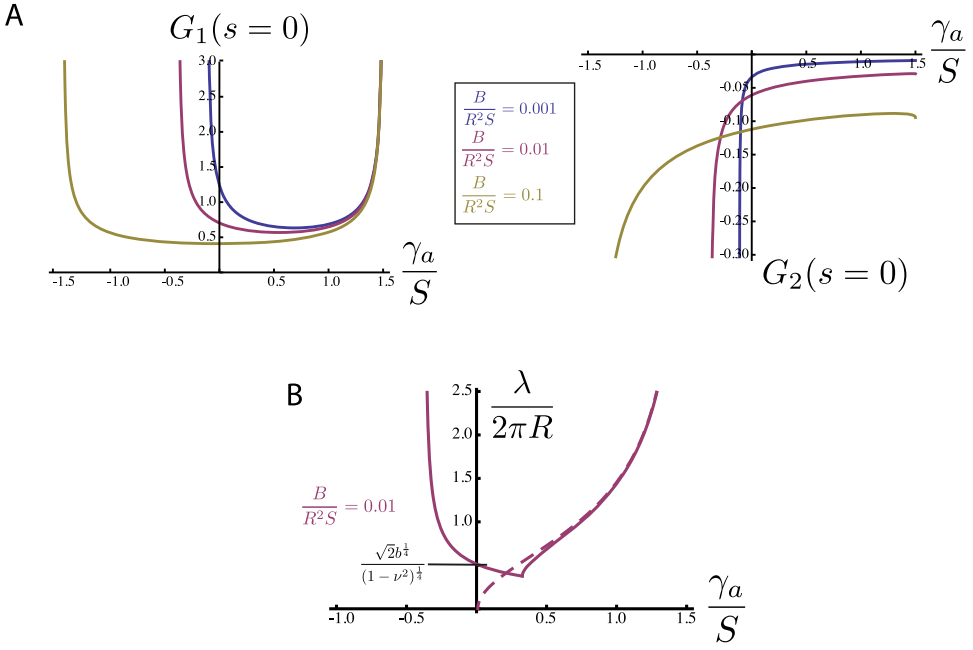

Figure D1. (A) Maximum values of the functions G_1 and G_2 introduced in appendix D as a function of $g = \frac{t_a}{S}$ for $\nu = \frac{1}{2}$ and different values of $b = \frac{B}{R^2S}$. The function $G_1(s=0)$ diverges when the cylindrical shell becomes unstable (see figure 3), whereas $G_2(s=0)$ diverges only near the buckling instability. (B) Maximum decay length of the functions G_1 and G_2 as a function of $\frac{t_a}{S}$ and for $\nu = \frac{1}{2}$. Dotted line: asymptotic value $\lambda = 2\pi R\frac{g}{2(1-\nu^2)-g}$ for $b \to 0$ and large g.

$$G_{t\phi}(s) = \frac{G_1(s)}{S} \tag{D.11}$$

$$G_{ms}(s) = \frac{R}{B}G_2(s) \tag{D.12}$$

$$G_{m\phi}(s) = 0. \tag{D.13}$$

It is straightforward to generalize this calculation to the case of a cylinder subjected to an anisotropic active tension t_a^s and t_a^ϕ. In that case, the functions G_1 and G_2 are modified to

$$G_1(q) = \frac{1}{2b(Rq)^4 + (g^s - 2\nu b)(Rq)^2 + (2(1-\nu^2) - g^\phi)} \tag{D.14}$$

$$G_2(q) = \frac{-b(Rq)^2}{2b(Rq)^4 + (g^s - 2\nu b)(Rq)^2 + (2(1-\nu^2) - g^\phi)} \tag{D.15}$$

with $g^s = \frac{t_a^s}{S}$ and $g^\phi = \frac{t_a^\phi}{S}$.

Finally, we note that this calculation can also be applied to obtain the Green functions for a passive cylinder subjected to an external pressure, deforming it away from its reference state. Indeed, the calculation of the Green function performed here only assumes that the cylinder is initially in a state of prestress. It is then easy to find the Green function of a uniformly deformed

elastic cylinder without active tension by replacing t_a^s and t_a^ϕ with elastic tensions generated by the deformation of the cylinder.

Appendix E. Coefficients of the shape differential equation for a shell of revolution

In this appendix, we give the expressions for the coefficients a_i, b_i, c_i and d_i introduced in equations (31)–(32).

$$
\begin{aligned}
a_0 &= -2\left(\frac{B\partial_s\psi\left((\nu+1)\sin\psi\cos^2\psi - r^3\partial_s^3\psi\psi\right)}{r^3} + \partial_s\psi\frac{B\left(\nu\partial_s\psi^2\sin\psi - \partial_s^2\psi\cos\psi\right)+\nu S\sin\psi}{r}\right.\\
&\quad \left. + \frac{B\left(\partial_s\psi\right)^2((1-2\nu)\cos 2\psi+1)+2S\cos^2\psi}{2r^2}\right)\\
a_1 &= \frac{B\nu\partial_s\psi\sin 2\psi + 2Br^2\partial_s\psi\partial_s^2\psi + 2r\cos\psi\left(B\nu\left(\partial_s\psi\right)^2+S\right)}{r^2}\\
a_2 &= 2S\\
b_0 &= 2\left(\frac{B(\nu+1)\partial_s\psi\sin^2\psi\cos\psi - r^3\partial_s^2\psi\left(S-2B\left(\partial_s\psi\right)^2\right) - r^2\partial_s\psi\cos\psi\left(B(\nu-1)(\partial_s\psi^2+S\right)}{r^3}\right.\\
&\quad \left. + \sin\psi\cos\psi\frac{S-2B\nu\left(\partial_s\psi\right)^2}{r^2}\right)\\
b_1 &= -\frac{2\left(B\partial_s\psi\left(\nu\sin^2\psi+\cos^2\psi\right)+r^2\partial_s\psi\left(S-B\left(\partial_s\psi\right)^2\right)+\nu r\sin\psi\left(B\left(\partial_s\psi\right)^2+S\right)\right)}{r^2}\\
b_2 &= \frac{2B\partial_s\psi\cos\psi}{r}\\
b_3 &= 2B\partial_s\psi\\
c_0 &= \frac{-4B(\nu+1)\sin\psi\cos^3\psi - 2Br^4\psi^{(4)}(s)}{r^4}\\
&\quad + 2\frac{B\nu\left(\partial_s\psi\right)^3\cos\psi - 2B\partial_s^3\psi\cos\psi + \partial_s\psi\left(B(2\nu+1)\partial_s^2\psi\sin\psi+\nu S\cos\psi\right)}{r}\\
&\quad + \frac{B\partial_s^2\psi((1-2\nu)\cos 2\psi+1)+2B(2\nu-1)\left(\partial_s\psi\right)^2\sin 2\psi + S\sin 2\psi}{r^2}\\
&\quad + \frac{Br\partial_s\psi\cos\psi((5\nu+2)\cos 2\psi-\nu-2)}{r^4}
\end{aligned}
$$

$$
\begin{aligned}
c_1 &= 2\Bigg(\frac{B(2\nu+1)\sin\psi\cos^2\psi + r^3\left(S\partial_s\psi - 2B\partial_s^3\psi\right)}{r^3} \\
&\quad + \frac{-B(\nu+2)\partial_s^2\psi\cos\psi + 2B\nu\left(\partial_s\psi\right)^2\sin(\psi) + \nu S\sin(\psi)}{r} - \frac{1}{2}B\partial_s\psi\frac{(4\nu-1)\cos 2\psi - 1}{r^2}\Bigg) \\
c_2 &= -\frac{2B\left(\nu\sin(\psi)\cos\psi + r^2\partial_s\psi' + \nu r\partial_s\psi\cos\psi\right)}{r^2} \\
c_3 &= 0 \\
d_0 &= \frac{B(\nu+1)\sin^2(2\psi) - 2r^4\left(2B\psi^{(3)}(s)\partial_s\psi + 2B\left(\partial_s^2\psi\right)^2 + S\left(\partial_s\psi\right)^2\right)}{r^4} \\
&\quad - 2\partial_s\psi\frac{-2B(\nu-2)\partial_s^2\psi\cos(\psi) + B(\nu-1)\left(\partial_s\psi\right)^2\sin\psi + 2\nu S\sin\psi}{r} \\
&\quad + \frac{2B\nu\partial_s^2\psi\sin 2\psi + 4B\nu\left(\partial_s\psi\right)^2\cos 2\psi - 2S\sin^2\psi}{r^2} \\
&\quad - B\frac{\partial_s\psi\sin\psi((5\nu+3)\cos 2\psi + 3\nu + 1)}{r^3} \\
d_1 &= 2B\Big(\frac{\cos\psi(\nu\cos 2\psi - \nu - 1) - 4r^3\partial_s\psi\partial_s^2\psi}{r^3} \\
&\quad + \frac{\nu\partial_s^2\psi\sin\psi + 2(\nu-1)\left(\partial_s\psi\right)^2\cos\psi}{r} + (2\nu-1)\frac{\partial_s\psi\sin 2\psi}{r^2} \\
d_2 &= \frac{2B\left(\nu\sin^2\psi - r^2\left(\partial_s\psi\right)^2 + (\nu+1)r\partial_s\psi\sin\psi + \cos^2\psi\right)}{r^2} \\
d_3 &= -\frac{4B\cos\psi}{r} \\
d_4 &= -2B.
\end{aligned}
$$

Appendix F. Sensitivity analysis

In this appendix, we detail our error estimation method and perform a sensitivity analysis of the method we use to extract the model parameters.

The mean value and standard error of the geometric parameters used to characterize cell shape are given in table 1. We start by detailing how the length L and mean curvature C of the shell in its initial resting state, before detachment, can be obtained from the measurements of the contact radius r_i and the middle cell contact angle ψ_i. We define the function $\mathcal{F}(r_i, \psi_i, C, L) = (\mathcal{F}_1, \mathcal{F}_2) = (\cos(\psi(L/2)), \int_0^L \pi r^2 \sin\psi\, ds - V)$, where $r(s)$ and $\psi(s)$ are the solutions of the shape equation (24) ($\frac{\sin\psi}{r} + \partial_s\psi = C$, $\cos\psi = \partial_s r$), for initial radius

$r(0) = r_i$ and angle $\psi(0) = \psi_i$. The integral $\int_0^L \pi r^2(s) \sin\psi(s) ds$ is the volume enclosed in this surface, and V is the mean volume of ectoderm cells. Solving for $\mathcal{F} = 0$ for a given (r_i, ψ_i) allows to find the length and mean curvature of the shell. To estimate the error on this evaluation, we write that a small perturbation on the input parameters $(dr_i, d\psi_i)$ modifies the value of the output values by dC and dL such that $\mathcal{F}(r_i + dr_i, \psi_i + d\psi_i, C + dC, L + dL) = 0$. The variation on output values can then be expressed as follows:

$$\begin{pmatrix} \frac{dC}{C} \\ \frac{dL}{L} \end{pmatrix} \simeq \mathbf{M}_{\mathcal{F}} \begin{pmatrix} \frac{dr_i}{r_i} \\ \frac{d\psi_i}{\psi_i} \end{pmatrix}, \tag{F.1}$$

with $\mathbf{M}_{\mathcal{F}} = -\mathbf{A}_{\mathcal{F}}^{-1}.\,\mathbf{B}_{\mathcal{F}}$,

$$\mathbf{A}_{\mathcal{F}} = \begin{pmatrix} L\frac{\partial \mathcal{F}_1}{\partial L} & C\frac{\partial \mathcal{F}_1}{\partial C} \\ L\frac{\partial \mathcal{F}_2}{\partial L} & C\frac{\partial \mathcal{F}_2}{\partial C} \end{pmatrix} \text{and } \mathbf{B}_{\mathcal{F}} = \begin{pmatrix} r_i\frac{\partial \mathcal{F}_1}{\partial r_i} & \psi_i\frac{\partial \mathcal{F}_1}{\partial \psi_i} \\ r_i\frac{\partial \mathcal{F}_2}{\partial r_i} & \psi_i\frac{\partial \mathcal{F}_2}{\partial \psi_i} \end{pmatrix}.$$

Numerical evaluation of these matrices for C and L satisfying $\mathcal{F} = 0$ yields

$$\mathbf{M}_{\mathcal{F}} = \begin{pmatrix} -0.38 & -0.05 \\ -0.11 & 0.07 \end{pmatrix}. \tag{F.2}$$

Assuming that the input variables are independent and normally distributed, the covariance matrix of output variables is then given by $\mathbf{Co}_{\mathcal{F}} = \mathbf{M}_{\mathcal{F}}.\,\mathbf{V}_{\mathcal{F}}.\,\mathbf{M}_{\mathcal{F}}^t$, with $\mathbf{V}_{\mathcal{F}} = \begin{pmatrix} \frac{\sigma_{r_i}^2}{r_i^2} & 0 \\ 0 & \frac{\sigma_{\psi_i}^2}{\psi_i^2} \end{pmatrix}$ the covariance matrix for the measurements of r_i and ψ_i. In addition, the matrix $\mathbf{M}_{\mathcal{F}}$ gives an estimate of the sensitivity of output parameters to the intput parameters: we find here that the curvature estimate is more sensitive to experimental errors than the length of the shell.

We now evaluate the variance on the stretching and bending modulus obtained by the minimization of the objective function $\mathcal{S}(\psi_i, r_i, \theta_s, \theta_s', \theta_b, \theta_i, \Delta r_b, \Delta r_i, S, B)$ defined in equation (47). Denoting the input variables of $\mathcal{S}$ are $x_\alpha = (\psi_i, r_i, \theta_s, \theta_s', \theta_b, \theta_i, \Delta r_b, \Delta r_i, \psi'(s_i), \psi'(s_f))$ and the output variables are $y_\alpha = (S, B)$. The optimal output variables y^* are found by minimizing the objective function, such that $\partial_y \mathcal{S}|_{y=y^*} = 0$. Following the approach previously introduced, we define the second-order derivative matrices $\mathbf{A}_{\mathcal{S}_{\alpha,\beta}} = y_\beta^* \partial^2 S/\partial y_\beta \partial y_\alpha$ and $\mathbf{B}_{\mathcal{S}_{\alpha,\beta}} = x_\beta \partial^2 S/\partial x_\beta y_\alpha$. The uncertainty in output parameters can then be evaluated from

$$\begin{pmatrix} \frac{dS}{S} \\ \frac{dB}{B} \end{pmatrix} \simeq \mathbf{M}_S \left(\frac{d\psi_i}{\psi_i} \frac{dr_i}{r_i} \frac{d\theta_s}{\theta_s} \frac{d\theta'_s}{\theta'_s} \frac{d\theta_b}{\theta_b} \frac{d\theta_i}{\theta_i} \frac{d\Delta r_b}{r_b} \frac{d\Delta r_i}{r_i} \frac{d\psi'(s_i)}{\psi'(s_i)} \frac{d\psi'(s_f)}{\psi'(s_f)} \right)^{\mathrm{t}}, \tag{F.3}$$

with $\mathbf{M}_S = -\mathbf{A}_S^{-1}.\,\mathbf{B}_S$. We find for the matrix $\mathbf{M}_S$:

$$\mathbf{M}_S = \begin{pmatrix} -0.26 & -0.95 & 0.08 & 0.09 & 0.01 & 0.01 & 0.004 & 0.003 & 0.01 & 0.04 \\ -0.71 & 0.25 & -0.18 & -0.01 & -0.03 & 0.02 & 0.002 & -0.004 & -0.08 & -0.04 \end{pmatrix}. \tag{F.4}$$

The variances of S and B are the square roots of the diagonal elements of the 2×2 matrix $\mathbf{Co}_S = \mathbf{M}_S \cdot \mathbf{V}_S \cdot \mathbf{M}_S^t$, with $\mathbf{V}_S$ the covariance matrix of input parameters, estimated from the standard deviation of experimental measurements (table 1). Furthermore, the matrix $\mathbf{M}_S$ gives an estimate of the sensitivity of output parameters S and B to the input parameters. It appears that the outcome is essentially sensitive to measurement of the deformation near the remaining contact cell (angle ψ_i and deformation dr_i).

Appendix G. Experimental methods

The cell-triplet assay (figure 5(A)) is performed as follows. Ectoderm progenitors are obtained from three to six mechanically dissociated zebrafish embryos, which were micro-injected with 100 pg *lefty1* mRNA at the one cell stage, placing them into DMEM/F12 culture medium. Glass micropipettes are pulled from glass capillaries and forged to ~3.5 μm radius and bent to ~45° angle before being passivated with heat-inactivated fetal bovine serum for seven minutes at room temperature. The micropipettes are then connected to a microfluidic flow control system, with negative pressure ranging from 7–750 Pa, a pressure accuracy of 7 Pa, and change rate of 200 Pas^{-1} on two independent channels. Micropipette movement and pressure are controlled via a custom-programmed interface.

References

[1] Salbreux G, Charras G and Paluch E 2012 Actin cortex mechanics and cellular morphogenesis *Trends Cell Biol* **22** 536–45

[2] Kruse K, Joanny J F, Jülicher F, Prost J and Sekimoto K 2005 Generic theory of active polar gels: a paradigm for cytoskeletal dynamics *Eur. Phys. J. E Soft Matter* **16** 5–16

[3] Love A E 1927 *Treatise on the Mathematical Theory of Elasticity* (Cambridge: Cambridge University Press)

[4] Timoshenko S, Woinowsky-Krieger S and Woinowsky S 1959 *Theory of Plates and Shells* (New York: McGraw-Hill)

[5] Guven J 2006 Laplace pressure as a surface stress in fluid vesicles *J. Phys. A: Math. Gen* **39** 3771

[6] Landau L D and Lifshitz E M 1986 *Theory of Elasticity* (Oxford: Butterworth-Heinemann)

[7] Salbreux G, Prost J and Joanny J F 2009 Hydrodynamics of cellular cortical flows and the formation of contractile rings *Phys. Rev. Lett.* **103** 058102

[8] Delaunay C H 1841 Sur la surface de révolution dont la courbure moyenne est constante *J. Math. Pures Appl.* 309–14

[9] Mayer M, Depken M, Bois J S, Jülicher F and Grill S W 2010 Anisotropies in cortical tension reveal the physical basis of polarizing cortical flows *Nature* **467** 617–21
[10] Eggers J 1997 Nonlinear dynamics and breakup of free-surface flows *Rev. Mod. Phys.* **69** 865–930
[11] Hannezo E, Prost J and Joanny J-F 2012 Mechanical instabilities of biological tubes *Phys Rev Lett* **109** 018101
[12] Borghi N and Nelson W J 2009 Intercellular adhesion in morphogenesis: molecular and biophysical considerations *Curr. Top. Devel. Biol.* **89** 1–32
[13] Maître J-L, Berthoumieux H, Krens S F G, Salbreux G, Jülicher F, Paluch E and Heisenberg C-P 2012 Adhesion functions in cell sorting by mechanically coupling the cortices of adhering cells *Science* **338** 253–6
[14] Maître J-L and Heisenberg C-P 2011 The role of adhesion energy in controlling cell-cell contacts *Curr. Opinion Cell Biol.* **23** 508–14
[15] Daoudi M, Lavergne E, Garin A, Tarantino N, Debré P, Pincet F, Combadière C and Deterre P 2004 Enhanced adhesive capacities of the naturally occurring Ile249–Met280 variant of the chemokine receptor CX3CR1 *J. Biol. Chem.* **279** 19649–57
[16] Chu Y-S, Thomas W A, Eder O, Pincet F, Perez E, Thiery J P and Dufour S 2004 Force measurements in e-cadherin-mediated cell doublets reveal rapid adhesion strengthened by actin cytoskeleton remodeling through rac and cdc42 *J. Cell. Biol.* **167** 1183–94
[17] Stoer J and Bulirsch R 2002 *Introduction to Numerical Analysis* vol 12 (Berlin: Springer)
[18] Timoshenko S and Gere J M 2012 *Theory of Elastic Stability* (New York: Dover)
[19] Ventsel E and Krauthammer T 2001 *Thin Plates and Shells: Theory, Analysis, and Applications* (Boca Raton, FL: CRC Press)
[20] Audoly B and Pomeau Y 2010 *Elasticity and Geometry: from Hair Curls to the Non-Linear Response of Shells* (Oxford: Oxford University Press)
[21] Lidmar J, Mirny L and Nelson D R 2003 Virus shapes and buckling transitions in spherical shells *Phys. Rev.* E **68** 051910
[22] Katifori E, Alben S, Cerda E, Nelson D R and Dumais J 2010 Foldable structures and the natural design of pollen grains *Proc. Natl Acad. Sci.* **107** 7635–9
[23] Levayer R and Lecuit T 2012 Biomechanical regulation of contractility: spatial control and dynamics *Trends Cell. Biol.* **22** 61–81
[24] Tinevez J-Y, Schulze U, Salbreux G, Roensch J, Joanny J-F and Paluch E 2009 Role of cortical tension in bleb growth *Proc. Natl Acad. Sci. USA* **106** 18581–6
[25] Clark A G, Dierkes K and Paluch E K 2013 Monitoring actin cortex thickness in live cells *Biophys. J.* **105** 570–80
[26] Krieg M, Arboleda-Estudillo Y, Puech P-H, Käfer J, Graner F, Müller D J and Heisenberg C-P 2008 Tensile forces govern germ-layer organization in zebrafish *Nature Cell Biol.* **10** 429–36
[27] Wu H W, Kuhn T and Moy V T 1998 Mechanical properties of l929 cells measured by atomic force microscopy: effects of anticytoskeletal drugs and membrane crosslinking *Scanning* **20** 389–97
[28] Paluch E and Heisenberg C-P 2009 Biology and physics of cell shape changes in development *Curr. Biol.* **19** R790–9
[29] Charras G T, Coughlin M, Mitchison T J and Mahadevan L 2008 Life and times of a cellular bleb *Biophys. J* **94** 1836–53
[30] Solon J, Kaya-Copur A, Colombelli J and Brunner D 2009 Pulsed forces timed by a ratchet-like mechanism drive directed tissue movement during dorsal closure *Cell* **137** 1331–42
[31] Lecuit T and Lenne P-F 2007 Cell surface mechanics and the control of cell shape, tissue patterns and morphogenesis *Nat. Rev. Mol. Cell. Biol.* **8** 633–44
[32] Farhadifar R, Röper J-C, Aigouy B, Eaton S and Jülicher F 2007 The influence of cell mechanics, cell–cell interactions, and proliferation on epithelial packing *Curr. Biol.* **17** 2095–104

[33] Kölsch V, Seher T, Fernandez-Ballester G J, Serrano L and Leptin M 2007 Control of drosophila gastrulation by apical localization of adherens junctions and rhogef2 *Science* **315** 384–6
[34] Schlichting K and Dahmann C 2008 Hedgehog and dpp signaling induce cadherin cad86c expression in the morphogenetic furrow during drosophila eye development *Mechanisms Devel.* **125** 712–28
[35] Larsen C W, Hirst E, Alexandre C and Vincent J-P 2003 Segment boundary formation in drosophila embryos *Development* **130** 5625–35
[36] Sawyer J M, Harrell J R, Shemer G, Sullivan-Brown J, Roh-Johnson M and Goldstein B 2010 Apical constriction: a cell shape change that can drive morphogenesis *Devel. Biol.* **341** 5–19
[37] Rodriguez E K, Hoger A and McCulloch A D 1994 Stress-dependent finite growth in soft elastic tissues *J. Biomech.* **27** 455–67
[38] Goriely A and Amar M B 2005 Differential growth and instability in elastic shells *Phys. Rev. Lett.* **94** 198103
[39] Amar M B and Goriely A 2005 Growth and instability in elastic tissues *J. Mech. Phys. Solids* **53** 2284–319
[40] Dervaux J and Amar M B 2008 Morphogenesis of growing soft tissues *Phys. Rev. Lett.* **101** 068101